Dynamics of Sheared Convective Boundary Layer Entrainment. Part I: Methodological Background and Large-Eddy Simulations

ROBERT J. CONZEMIUS*

School of Meteorology, University of Oklahoma, Norman, Oklahoma, and Department of Atmospheric Science, Colorado State University, Fort Collins, Colorado

EVGENI FEDOROVICH

School of Meteorology, University of Oklahoma, Norman, Oklahoma

ABSTRACT

The reported study examines the dynamics of entrainment and its effects on the evolution of the dry atmospheric convective boundary layer (CBL) when wind shear is present. The sheared CBL can be studied by means of direct measurements in the atmosphere, laboratory studies, and numerical techniques. The advantages and disadvantages of each technique are discussed in the present paper, which also describes the methodological background for studying the dynamics of entrainment in sheared CBLs. For the reported study, large-eddy simulation (LES) was chosen as the primary method of convective entrainment investigation. Twenty-four LES runs were conducted for CBLs growing under varying conditions of surface buoyancy flux, free-atmospheric stratification, and wind shear. The simulations were divided into three categories: CBL with no mean wind (NS), CBL with a height-constant geostrophic wind of 20 m s^{-1} (GC), and CBL with geostrophic wind shear (GS). In the simulated cases, the sheared CBLs grew fastest, relative to the NS CBLs, when the surface buoyancy flux was weak and the atmospheric stratification was moderate or weak.

Three fundamental findings resulted from the investigated CBL cases: (i) the entrainment zone shear is much more important than the surface shear in enhancing CBL entrainment, although entrainment zone shear is indirectly affected by surface shear; (ii) the sheared entrainment zone features a sublayer of nearly constant flux Richardson number, which points to a balance between shear production and buoyancy consumption of turbulence kinetic energy (TKE) that regulates entrainment; and (iii) the fraction of entrainment zone shear-generated TKE spent on the entrainment is lower than suggested by earlier studies.

1. Introduction

The atmospheric boundary layer (ABL) is the essentially turbulent lower layer of the atmosphere that is sensitive to surface fluxes of momentum, temperature and passive scalars on time scales of about an hour or less (Stull 1988). In the ABL with dominant convective forcing, which is the case of so-called atmospheric convective boundary layer (CBL), turbulence is primarily forced either by the heating at the underlying surface or radiative cooling in clouds at the top of the layer, or by both mechanisms. If the CBL has no clouds, it is referred to as a dry (or clear) CBL (Holtslag and Duynkerke 1998), and the main driving mechanism for turbulence in the layer is heating at the lower surface. The dry atmospheric CBL is the subject of this study.

To facilitate discussion throughout the rest of this text, we will consider three (sub) layers typically distinguished within the CBL (Stull 1988). In each of these layers, the meteorological quantities will be regarded as horizontally or temporally averaged. The surface layer is the lowest sublayer, which comprises approximately 10% of the total CBL depth, where the lower surface limits the vertical extent of convective motions, and a superadiabatic temperature lapse rate is found. The main portion of the CBL is occupied by the mixed layer, often referred to as the CBL interior, in which

* Current affiliation: Windlogics, Inc., Grand Rapids, Minnesota.

Corresponding author address: Robert J. Conzemius, Windlogics, Inc., 201 NW 4th Street, Grand Rapids, MN 55744.
E-mail: robert.conzemius@att.net

mixing by stronger vertical motions typically keeps the vertical potential temperature gradients very small. At the CBL top is the entrainment zone, often referred to as the interfacial layer, where stable stratification inhibits vertical mixing and the temperature gradients once again become large. Above the CBL is the free atmosphere, whose stratification, generally speaking, can be in a range from almost neutral to moderately stable.

Among a multitude of processes that can influence CBL evolution, this study focuses specifically on entrainment, the process by which more highly buoyant air from the free atmosphere is engulfed by the CBL air and, as a result, becomes part of the CBL air (Randall and Schubert 2004). Other processes that may influence the CBL development, such as horizontal convergence of the flow within the CBL (Stull 1988; Fedorovich and Thäter 2001) and differential temperature advection (Sorbjan 2004), will not be considered here.

Entrainment regulates the exchange of momentum and scalars (such as water vapor and pollutants) between the CBL and the overlying free atmosphere. Numerical weather prediction (NWP) models rely on the accurate characterization of the horizontal and vertical distributions of water vapor in the atmosphere, which are highly influenced by entrainment. For air pollutants, a deeper CBL enables greater dilution of pollutants that are released near the ground (Lyons and Scott 1990), so entrainment also plays an important role in the dispersion of air pollutants. Finally, entrainment can have a strong influence on the wind profiles within the CBL (Hoxit 1974; Arya and Wyngaard 1975; LeMone et al. 1999).

Although in most cases, the CBL entrainment is originally and primarily driven by heating from the surface, a purely buoyancy-driven CBL rarely exists, and there are many CBL cases in which the surface heating is weak while the shear production of turbulence is relatively strong. In these cases, the shear effects on CBL entrainment cannot be ignored. To date, many studies of entrainment have focused on the shear-free CBL, and theories for shear-free entrainment have been reasonably well tested in laboratory experiments, through atmospheric measurements, and by numerical simulations. Far fewer studies have been performed on the influence of wind shear on CBL entrainment, and most of the theories and parameterizations developed from those studies have not been tested over a suitably wide range of atmospheric conditions. The goal of the present study is to examine the dynamics of entrainment in the CBL with wind shears and to comprehensively test existing hypotheses and parameterizations regarding the effects of wind shear on entrainment and, more generally, on the CBL development.

Results of the study are reported in two separate articles. This article (Part I) develops the methodology for studying the dynamics of entrainment in sheared CBLs and presents an analysis of the dynamics of the sheared convective boundary layer as reproduced by large-eddy simulations (LES) of the sheared CBL. In Conzemius and Fedorovich (2006, hereafter Part II), several existing entrainment parameterizations for the sheared CBL are tested against the LES results from Part I.

2. Background

a. Underlying conceptual framework

The growth of the CBL through entrainment can be conceptualized most easily within an ensemble-averaging framework. In theory, an ensemble average implies averaging over an infinite number of realizations of the considered flow (Pope 2000). In the horizontally (quasi) homogeneous CBL, horizontal averages may be taken as substitutes for the ensemble averages, and the horizontally averaged buoyancy and turbulence fields can be considered as functions of time and height only.

We will base our discussion on the CBL horizontally averaged profiles of buoyancy $\bar{b} = g/\theta_0(\bar{\theta} - \theta_0)$, buoyancy flux $B = (g/\theta_0)\overline{w'\theta'} = \overline{w'b'}$, horizontal velocity components $\bar{u}$ and $\bar{v}$, and corresponding turbulent shear stress components (negatives of the momentum flux components normalized by density), $\tau_x = -\overline{w'u'}$ and $\tau_y = -\overline{w'v'}$, where g is the gravitational acceleration, θ is potential temperature, θ_0 its reference value (to account for the presence of water vapor, θ could refer to virtual potential temperature; we use $\theta_0 = 300$ K), w is vertical velocity, overbars denote horizontal averages, and primes indicate deviations from horizontal averages.

From this point forward, horizontal averages will be assumed, and overbars will be dropped in the notation for velocity and temperature/buoyancy averages. By neglecting mean vertical motion at the CBL top, the evolution of the average buoyancy profile in the CBL can be described entirely in terms of its vertical turbulent flux, and the evolution of the turbulence kinetic energy (TKE) profile can be described in terms of the sources (buoyancy flux and shear production), transport (by velocity fluctuations and pressure), and the viscous dissipation of TKE (Lilly 1968; Zilitinkevich 1991). The entrainment rate is essentially determined by a balance among these sources and sinks of energy.

In the dry, shear-free CBL, the surface buoyancy flux is the only turbulence production mechanism, and the entrainment rate is determined by the portion of the

buoyancy-generated TKE that is available for the TKE-consuming process of entrainment. The remaining TKE is converted into thermal energy through the turbulence cascade process and viscous dissipation. The earliest study of entrainment (Ball 1960) neglected dissipation and assumed that 100% of the TKE was available for entrainment. Lilly (1968) realized that dissipation may be a significant sink of TKE and made estimates of entrainment based on the availability of buoyancy-generated TKE ranging from 0% to 100%. Since that time, numerous studies have attempted to determine this fraction (Betts 1973; Carson 1973; Tennekes 1973; Stull 1973; Zilitinkevich 1991; Fedorovich et al. 2004a). Its generally agreed-upon value for shear-free CBL is about 20%. When placed in the appropriate conceptual model context (e.g., within the zero-order model framework, see below), this ratio is equivalent to the entrainment flux ratio, that is, the ratio of the negative of the buoyancy flux minimum in the entrainment zone to the surface buoyancy flux.

For the sheared CBL, a similar problem exists regarding the ultimate sink of the shear-produced TKE, but the fraction of such shear-produced TKE available for entrainment is less well known than in the shear-free CBL case. Zeman and Tennekes (1977) attempted to account for the dissipation of shear-generated TKE in their entrainment equation, but no reliable data on such dissipation in sheared CBLs existed at that time, so they were unable to quantify it. Soon thereafter, Price et al. (1978) estimated the fraction of entrainment zone shear-generated TKE available for entrainment to be 0.7 based on their study of storm-induced mixed layer deepening in the ocean. This number has since been used in several other studies of sheared CBLs (Tennekes and Driedonks 1981; Driedonks 1982; Pino et al. 2003). It is reasonable to assume that, as the shear production of TKE increases and as long as some fraction of shear-produced TKE is available for entrainment, the entrainment flux ratio also increases from its established shear-free value of 0.2. Thus, the entrainment flux ratio can be used as an indicator of the relative effects of shear and buoyancy on the evolution of the CBL, with the increase in the ratio associated with the enhanced negative area in the buoyancy flux profile at the CBL top. Accordingly, if the change in the buoyancy flux profile due to the effects of shear is integrated over the depth of the CBL, the integral difference, as compared to the integral shear production of TKE, can be used as an estimate of the shear-produced TKE available for entrainment.

This fraction is apparently dependent on where the shear production of TKE occurs. Since turbulence effectively mixes momentum in the interior of the CBL, it is natural for the shear to accumulate at the surface and in the entrainment zone, so the availability of shear-produced TKE for entrainment can be determined separately for these two discrete sublayers of the sheared CBL. Surface shear-generated turbulence must be transported through the entire depth of the CBL, up to the entrainment zone, before it can be used to drive the entrainment process, and is therefore exposed to the energy cascade process along the entire route. On the other hand, turbulence produced by shear in the entrainment zone is immediately in a position to promote entrainment. Deardorff and Willis (1982) addressed the relative importance of surface shear and entrainment zone shear in their water tank studies, and their data suggested that both surface shear and interfacial layer shear promoted entrainment, but the effects of interfacial layer shear were found to be of primary importance.

b. Existing methods of estimating shear contribution to the CBL entrainment

Efforts to understand the evolution the CBL under conditions of significant shear have been made using atmospheric data, laboratory models, and numerical methods. Several atmospheric studies have focused on the effects of entrainment and CBL processes on the mean profiles of momentum using sounding data (Hoxit 1974; Arya and Wyngaard 1975; Garratt and Wyngaard 1982; LeMone et al. 1999; Angevine et al. 2001). Others have focused on the CBL turbulence structure in CBLs with wind shear at the surface (LeMone 1973; Pennel and LeMone 1974). Higher-order turbulent moments and their budgets, which can be used most directly to quantify the TKE budgets in the CBL, have been the focus of field campaigns using aircraft, tethersondes, or radar observations (Lenschow 1970, 1974; Kaimal et al. 1976; Caughey and Palmer 1979; Lenschow et al. 1980; Brost et al. 1982a,b; Chou et al. 1986; Flamant et al. 1997; Schneider and Lilly 1999). Some of the more recent studies have specifically estimated entrainment flux ratios under conditions of broadly varying surface heating and shear (Grossman 1992; Betts et al. 1992; Betts and Ball 1994; Betts and Barr 1996; Barr and Strong 1996; Davis et al. 1997; Flamant et al. 1997; Angevine 1999; Margulis and Entekhabi 2004), but the methods of analysis varied, and the scatter in their estimates of entrainment flux ratio as a function of entrainment zone shear indicates that other factors, not specifically addressed in those analyses, also influence the entrainment flux ratio. Yet another group of studies compared CBL depth estimates from balloonborne atmospheric soundings with en-

trainment equations accounting for shear contribution (Mahrt and Lenschow 1976; Stull 1976a,b,c; Zeman and Tennekes 1977; Tennekes and Driedonks 1981; Driedonks 1982; Boers et al. 1984; Batchvarova and Gryning 1991, 1994; Pino et al. 2003).

The greatest difficulty in using atmospheric data to quantify the shear effects on entrainment is that, during a field campaign, it is almost impossible to isolate the effects of the process being studied (in this particular case, entrainment) from the effects of other competing processes contributing to the CBL evolution, so the data reflect the cumulative effect of all the processes occurring simultaneously. Additionally, the second-order turbulent moments needed for the estimation of TKE budgets require long horizontal or temporal averaging, and these averages do not appear to converge quickly to an ensemble mean—the basis under which the averaged TKE budget equations have been obtained for the horizontally quasi-homogeneous CBL.

In laboratory (e.g., water tank) studies of CBL entrainment, conditions can be controlled to focus on the fluid process being studied. Numerous water tank entrainment experiments have been conducted over the past 40 years using turbulent boundary layers growing through stratified water. Some of these studies focused on the effects of heating of the lower surface (buoyancy production of TKE; Turner 1965; Deardorff et al. 1969, 1980; Willis and Deardorff 1974; Deardorff and Willis 1985). Others used mechanical agitation (Turner 1968) or shear applied at the upper surface (Kato and Phillips 1969; Wu 1973; Long 1975; Deardorff and Willis 1982) to produce turbulence. None of these experiments has been designed to investigate entrainment with both shear and buoyancy forcing occurring simultaneously.

Experiments focusing on the shear effects on entrainment in a horizontally evolving CBL have been conducted in the stratified wind tunnel of the University of Karlsruhe, Germany, in the 1990s (Fedorovich et al. 1996; Fedorovich and Kaiser 1998; Kaiser and Fedorovich 1998; Fedorovich et al. 2001a,b). These experiments have shown a significant dependence of CBL growth on the shear across the CBL top, but it was found out (Fedorovich and Thäter 2001) that horizontally evolving turbulent momentum fluxes resulted in flow divergence in the wind tunnel CBL model. This divergence directly competed with entrainment in influencing the CBL depth and was probably the dominant effect.

Entrainment can also be studied numerically. Following Wyngaard (1998), we will use term simulation for a numerical technique that resolves most of the energy-containing motions on the numerical grid and use the term model if the turbulent component of the flow motion is not resolved. Deardorff (1970a) pioneered the use of large-eddy simulation (LES: Pope 2000) for the study of the atmospheric CBL. Since then, the LES has become one of the most popular tools to study the CBL and has played an important role in the understanding of the dynamics of entrainment in the CBL (Deardorff 1974, 1980; Moeng and Wyngaard 1984; Wyngaard and Brost 1984; Mason 1989; Schmidt and Schumann 1989; Sorbjan 1996a,b; Lewellen and Lewellen 1998; Sullivan et al. 1998; vanZanten et al. 1999; Fedorovich et al. 2004a). For the sheared CBL, a number of LES studies have significantly advanced an understanding of its turbulence structure (Deardorff 1972; Sykes and Henn 1989; Khanna and Brasseur 1998; Kim and Park 2003), turbulence dynamics (Moeng and Sullivan 1994), velocity field statistics (Brown 1996), and turbulence spectra (Otte and Wyngaard 2001). None of the above studies, however, has focused directly on the entrainment in sheared CBLs.

Several recent LES studies of sheared CBLs have addressed the issue of sheared CBL entrainment more directly. Fedorovich et al. (2001a,b) numerically simulated the wind tunnel experiments mentioned above and compared their simulations with the wind tunnel data. Pino et al. (2003) conducted a three-case numerical study of the sheared CBL and compared the output of their LES runs with atmospheric CBL data and their proposed entrainment parameterization. Sorbjan (2004) developed a parameterization for the heat flux at the top of the sheared CBL and conducted several simulations of baroclinic CBLs to test the parameterization. Kim et al. (2003) analyzed the gradient Richardson number in the entrainment zone at the top of the sheared CBL and studied, in detail, the Kelvin–Helmholtz (KH) type structures in the entrainment zone, relating the KH wave breaking processes to episodes of enhanced entrainment.

Entrainment models based on the Reynolds-averaged Navier–Stokes (RANS) equations are commonly employed in NWP schemes. Moeng and Wyngaard (1989) and Ayotte et al. (1996) have evaluated the most popular multilevel RANS-based models of the CBL, so they will not be discussed here.

If one integrates the RANS equations for the horizontally homogeneous CBL over the depth of the CBL, the bulk model equations for the CBL are obtained. The bulk model framework can be used to quantify entrainment and to aid the conceptual understanding of processes influencing entrainment. The bulk CBL models are similar in how they describe the bulk properties of the CBL, but they differ in their degree of complexity in representation of the entrainment zone structure.

The simplest bulk model is the zero-order model

(ZOM: Lilly 1968;[1] Zilitinkevich 1991; Fedorovich 1995) in which the CBL is represented by a single layer of height-constant buoyancy and velocity. Stull (1976a,b,c), Zeman and Tennekes (1977), Tennekes and Driedonks (1981), Driedonks (1982), Boers et al. (1984), Batchvarova and Gryning (1991,1994), Fedorovich (1995), and Pino et al. (2003) have all derived sheared-entrainment equations within the ZOM framework.

The first-order model (FOM) (Betts 1974) is the lowest order model capable of resolving the buoyancy and velocity profiles in the entrainment zone. It has height-constant buoyancy and velocity in the CBL mixed layer and linearly changing buoyancy and velocity in the entrainment zone. Mahrt and Lenschow (1976) employed the FOM in their study of sheared CBLs. Sorbjan (2004) proposed a parameterization of sheared convective entrainment that requires at least first-order representation of the meteorological profiles throughout the entrainment zone. The dependence of sheared entrainment on entrainment zone Richardson number, predicted by Mahrt and Lenschow (1976) and confirmed by Kim et al. (2003) and Sorbjan (2004), suggests that one needs, as a minimum, FOM representation of the CBL structure in order to adequately capture the features of turbulence that regulate the entrainment process. However, in no cases has a complete set of FOM-based equations (without simplifying assumptions) been derived for the sheared CBL.

The general structure model (GSM) (Deardorff 1979; Fedorovich and Mironov 1995) is a higher-order bulk CBL model (it was developed so far only for the shear-free entrainment) that describes the entrainment zone profile of buoyancy with a higher-order polynomial. The particular form of this polynomial is determined by essentially geometrical (profile matching) and scaling considerations.

c. Shear sheltering of turbulence

In a more fundamental sense, there is no consensus in the boundary layer research community on whether mean shear enhances or suppresses entrainment. Shear across the CBL top can deform thermals so that they do not penetrate as effectively into the inversion; this can theoretically interfere with the entrainment process. If thermals are prevented from overshooting their equilibrium level, then the entrainment zone heat flux would be reduced, and the CBL growth would be slightly slower. If this effect dominates, the shear, in

essence, shelters the CBL from the free atmospheric air (Hunt and Durbin 1999). Although Fedorovich et al. (2004a, b) made some attempts to address this question, the present study hopes to provide some more conclusive answers to the problem of shear sheltering.

d. Remaining questions

Several other questions regarding the sheared CBL entrainment have not been sufficiently answered by the studies:

1) How does the entrainment rate depend on shear under a broad variety of atmospheric conditions?
2) Can the relative roles played by surface shear versus entrainment zone shear in modifying CBL entrainment be quantified?
3) What fraction of the shear-generated TKE is available for entrainment as opposed to being dissipated?
4) Given the results of Mahrt and Lenschow (1976), Kim et al. (2003, 2005, manuscript submitted to *Bound.-Layer Meteor.*), and Sorbjan (2004), how do the flux, gradient, and bulk Richardson numbers behave in the entrainment zone of sheared CBLs under different conditions, and could any one of them be used as a critical controlling parameter of the dynamics of sheared CBL entrainment?
5) How well do predictions of sheared entrainment by earlier proposed entrainment equations compare with LES predictions for characteristic atmospheric ranges of CBL buoyant and nonbuoyant forcings?

The first four questions will be addressed in the analyses of numerical simulation data presented in section 4. The answers to question 5) will be given in Part II. In order for the flow of logic in our presentation to be smooth, we believe it is first necessary to carefully clarify the methodology and analysis techniques that will form the framework of our study of sheared CBLs.

3. Methods

Based on the considerations presented in section 2, LES was selected as the primary investigation tool in the present study of entrainment in the sheared atmospheric CBL. The LES results have been analyzed in conjunction with predictions of the entrainment by bulk CBL models (ZOM and FOM). We believe the analyses of the bulk model entrainment data to be rather important because of the utility of these models in facilitating a conceptual understanding of the processes that are critical to the dynamics of sheared CBL entrainment.

---

[1] Lilly did not include velocity-field representation in his original version of the ZOM.
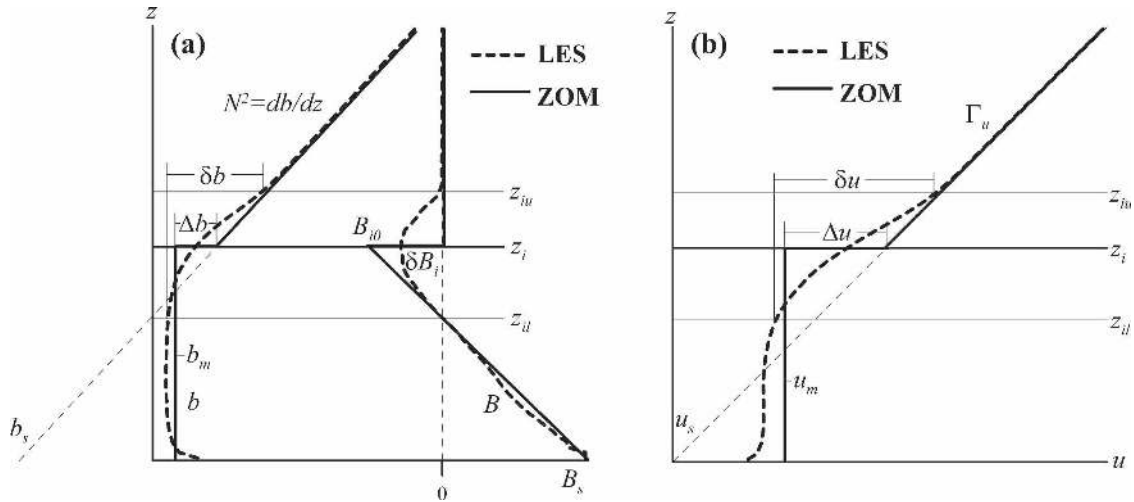
FIG. 1. Profiles of (a) buoyancy and buoyancy flux and (b) momentum in the horizontally homogeneous CBL. Heavy dashed lines indicate realistic horizontally averaged profiles, and heavy solid lines indicate their representation in the zero-order jump model. Lighter solid lines are the lower (z_{il}) and upper (z_{iu}) limits of the entrainment zone. The diagonal dashed line in (b) represents the profile of geostrophic wind.

a. Zero-order model

In the ZOM, the CBL is represented by a single layer of height-constant buoyancy and velocity, defined as

$$b_m = \frac{1}{z_i} \int_0^{z_i} b \, dz, \quad u_m = \frac{1}{z_i} \int_0^{z_i} u \, dz, \quad v_m = \frac{1}{z_i} \int_0^{z_i} v \, dz.$$

(1)

Figure 1 shows the CBL structure adopted in the ZOM and compares it with actual (in this case LES) profiles of horizontally averaged buoyancy, buoyancy flux, and velocity. At the CBL top in the ZOM are zero-order discontinuities in buoyancy, Δb, and velocity components, Δu and Δv. Above the CBL, in the free atmosphere, the buoyancy changes at a linear rate of $\partial b/\partial z = N^2$, where N is the Brunt–Väisälä frequency. The velocity components also have a linear dependence on height in the free atmosphere: $\partial u/\partial z = \Gamma_u$ and $\partial v/\partial z = \Gamma_v$. Note that the LES buoyancy flux profiles change gradually between the lower (z_{il}) and upper (z_{iu}) limits of the entrainment zone (which is defined as the layer of negative B), whereas the B interface in the ZOM is sharp.

b. Entrainment flux ratio as comparison criterion

To address the sheared CBL entrainment problem, an appropriate framework for comparison with shear-free CBLs must first be established. Because shear-free CBLs growing in linear stratification backgrounds of different strength all have a common entrainment flux ratio of about 0.2 when analyzed within the conceptual framework of the ZOM (Fedorovich et al. 2004a), we have chosen this flux ratio as the comparison criterion.

However, if the local value of the heat flux at the CBL top is used to calculate the entrainment flux ratio, the value of that ratio in LES ($-\delta B_i/B_s$) is smaller than it is in the ZOM ($-B_{i0}/B_s$), and the LES entrainment flux ratio is stratification-dependent (Fedorovich et al. 2004a), despite the fact that the integral parameters of entrainment (e.g., the CBL depth growth rate) predicted by both techniques may be the same. This difference complicates interpretation of the LES results in terms of the fraction of buoyancy-produced TKE spent on entrainment.

A way to look at the difference between the ZOM and actual buoyancy flux profiles is discussed in Lilly (2002a,b), who suggested that, locally, the interface remains sharp as in the ZOM but that the height of the interface is locally variable. However, LES (Sullivan et al. 1998; Kim et al. 2003) and atmospheric data (Kiemle et al. 1995) suggest that the interface may not be sharp everywhere, at least in the case of the dry CBL. Rather, LES results (Fedorovich et al. 2004a) suggest that the ratio of the area of negative heat flux in the LES profile is nearly equal to that in the ZOM profile (Fig. 1a). Because the local ratios $-\delta B_i/B_s$ and $-B_{i0}/B_s$ do not express the integral properties of the interfacial layer, we propose, below, an integral technique intended to better quantify the bulk properties of entrainment.

When retrieved from the horizontally averaged LES B profiles, the areas of positive and negative B are respectively defined as
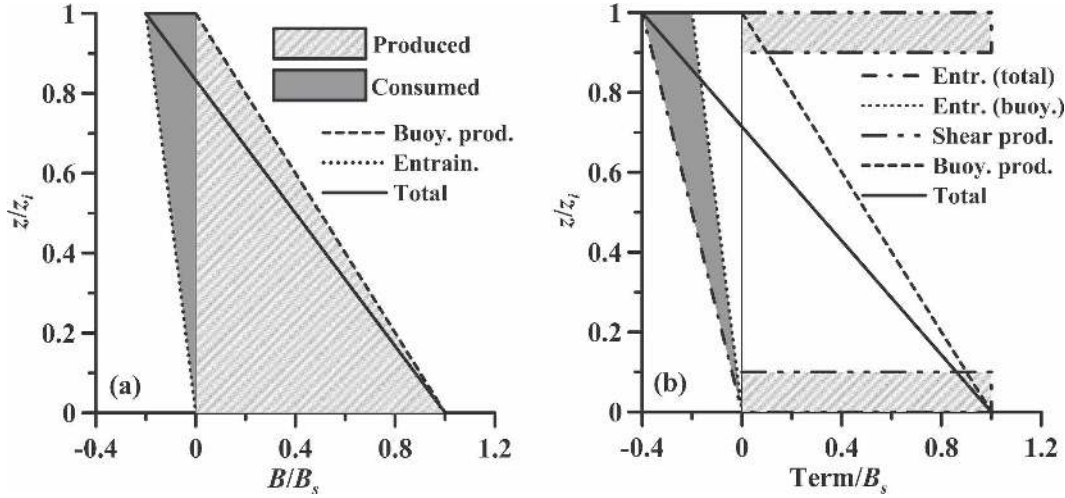
FIG. 2. Buoyancy flux profiles in the ZOM representation of the dry CBL using the process partitioning of vanZanten et al. (1999): (a) in the shear-free CBL, the dashed line represents the buoyancy flux due to heating at the lower surface (TKE production), the dotted line stands for the buoyancy flux of entrainment (TKE consumption), and the solid line is the total buoyancy flux; (b) in the sheared CBL, the dot–dot–dashed line represents the shear production of TKE, and the dot–dashed line represents the total entrainment, with the shaded area representing the buoyancy destruction of shear-produced TKE and the solid line representing the total buoyancy flux.

$$A_{PL} = \int_0^{z_{il}} B(z)\, dz; \quad A_{NL} = -\int_{z_{il}}^{z_{iu}} B(z)\, dz. \quad (2)$$

The analogous negative and positive areas can be calculated from the ZOM profiles. Defining $A_R = -B_{i0}/B_s$, the ZOM buoyancy flux profile can be written

$$B\left(\frac{z}{z_i}\right) = B_s\left[\left(1 - \frac{z}{z_i}\right) - A_R \frac{z}{z_i}\right]; \quad 0 \le z/z_i < 1. \quad (3)$$

At this point, we adopt for our analysis the process-partitioning concept developed by Manins and Turner (1978) and Stage and Businger (1981) and further explained in vanZanten et al. (1999). The buoyancy flux, which can be either a TKE generation or TKE destruction mechanism, is partitioned according to physical processes that shape the resulting buoyancy-flux profile (Fig. 2a). In the case of the dry, shear-free CBL, the buoyancy flux is a sum of heating from the lower surface (positive buoyancy flux) and the entrainment (negative buoyancy flux). If Eq. (3) is partitioned accordingly, the buoyancy flux due to surface heating, B_+, would be $B_+(z/z_i) = B_s(1 - z/z_i)$, where B_s is the surface buoyancy flux. The entrainment flux B_e would be $B_e(z/z_i) = -A_R B_s z/z_i$, where B_e is the buoyancy flux due to entrainment. If these two profiles are integrated separately, their negative and positive areas are $A_{NZ} = 0.5 A_R B_s z_i$ and $A_{PZ} = 0.5 B_s z_i$, respectively, and their ratio is exactly A_R. In this shear-free CBL context, the fraction $A_R = 0.2$ would imply that two-tenths of the

buoyancy-generated TKE from the surface heating is used for entrainment and the remaining eight-tenths is dissipated.

On the other hand, if the negative and positive portions of the total ZOM buoyancy profile (see Fig. 1) are integrated, the areas are

$$A_P = \int_0^{\frac{1}{1+A_R}z_i} B_s\left[\left(1 - \frac{z}{z_i}\right) - A_R \frac{z}{z_i}\right] dz = \frac{B_s z_i}{2(1 + A_R)}, \quad (4)$$

$$A_N = -\int_{\frac{1}{1+A_R}z_i}^{z_i} B_s\left[\left(1 - \frac{z}{z_i}\right) - A_R \frac{z}{z_i}\right] dz$$

$$= \frac{B_s z_i}{2(1 + A_R)} A_R^2, \quad (5)$$

where the limit of integration $[1/(1 + A_R)]z_i$ is the buoyancy-flux profile zero crossover height. The area ratio is $A_N/A_P = A_R^2$, which, for $A_R = 0.2$, yields $A_N/A_P = 0.04$. Thus, in the ZOM of shear-free CBL:

$$A_R = \sqrt{\frac{A_N}{A_P}} = \frac{A_{NZ}}{A_{PZ}}. \quad (6)$$

To retrieve A_R from the LES profiles, we may assume, at this point, that $A_{PL} = A_P$ and $A_{NL} = A_N$ (it will be

demonstrated in section 4 that such an assumption indeed holds for the shear-free CBL). That is, the integral negative and positive areas are the same in the LES as they are in the ZOM, as long as A_R, which in the shear-free case is interpreted as the fraction of buoyancy-generated TKE spent on entrainment (see above), is the same.

The use of (6) is only justified if the positive and negative buoyancy flux contributions vertically overlap. If these contributions occur in exclusive layers, (6) will overestimate A_R. Analyses of LES results do show that positive and negative areas indeed overlap throughout much of the entrainment zone and mixed layer in all studied CBL cases.

Expressing the entrainment flux ratio A_R in terms of (6), therefore, allows the interpretation of entrainment in terms of integral physical processes, which is expected to better quantify it than would the local LES entrainment flux ratio $-\delta B_i/B_s$. From this point forward, we shall refer to the shear-free equilibrium entrainment flux ratio as C_1 in order to distinguish it from the more general entrainment flux ratio A_R. The ratio C_1 has the meaning of the fraction of buoyancy-produced TKE used for entrainment in the shear-free CBL, and its value is 0.2, whereas the meaning of A_R changes when multiple physical processes contribute to entrainment.

c. Contribution of shear-generated TKE to the entrainment flux

In the case of the sheared CBL (see Fig. 2b), we consider two additional processes that act as sources and sinks of TKE: 1) shear production of TKE and 2) consumption of shear-generated TKE by entrainment. These processes can be illustrated by examining the integral TKE equation derived within the ZOM framework (Fedorovich 1995):

$$\frac{d}{dt}\int_0^{z_i} e\, dz = u_m\tau_{xs} + v_m\tau_{ys} + \frac{1}{2}(\Delta u^2 + \Delta v^2)\frac{dz_i}{dt}$$

$$+ \frac{z_i}{2}\left(B_s - \Delta b\frac{dz_i}{dt}\right) - \Phi_i - \int_0^{z_i} \varepsilon\, dz, \quad (7)$$

where e is the averaged (in the ensemble sense, see section 1) TKE, Φ_i is the flux due to upward radiation of energy from the top of the CBL, and ε the dissipation rate of TKE. The left-hand side of (7) represents the time rate of change of the integral of horizontally averaged TKE in the ZOM of the CBL. The first two terms on the right-hand side represent the surface shear

contribution to the integral TKE budget, with τ_{xs} and τ_{ys} being the surface values of τ_x and τ_y (their signs have been chosen to show that the surface shear terms are source terms). The third term represents the shear generation at the CBL top, and the fourth term represents the contribution to the integral TKE budget from the buoyancy production at the surface (B_s) and consumption of TKE by entrainment ($\Delta b dz_i/dt$). The shear-produced TKE, described by the first three terms in (7), can be consumed in the CBL (the left-hand side), by dissipation (the last term on the right-hand side), or by the entrainment (Φ_i is normally small under typical conditions in the atmospheric CBL; see Fedorovich et al. 2004a). If the increase in dissipation does not account for all the shear-generated TKE, the consumption associated with the entrainment, $\Delta b dz_i/dt$, should be larger than it would be for the shear-free CBL, and shear-generated TKE should be enhancing the entrainment.

Thus, integrating the change in the buoyancy flux profile from the shear-free buoyancy flux profile and taking the ratio of the integral change (the change in $\Delta b dz_i/dt$) to the integral shear production [the first three terms in Eq. (7)], we can come up with the fraction of shear-generated TKE that is available for entrainment (the ratio of the shaded area to the hatched area in Fig. 2b). Profiles of turbulent buoyancy flux result from the cumulative action of all these contributing processes: surface heating, entrainment due to buoyancy-generated TKE, and entrainment due to shear-generated TKE. Separating these contributions in an individual LES buoyancy flux profile requires some assumptions to be made.

First, we assume that the shear-generated TKE does not affect the fraction of buoyancy-generated TKE used for entrainment and vice versa. Assuming $C_1 = 0.2$ in sheared CBLs as it is in shear-free CBLs, a reference shear-free buoyancy flux profile can be calculated. The fraction of the shear-produced TKE being used for entrainment, C_P, can be determined by integrating, over the depth of the CBL, the difference between the sheared CBL buoyancy flux profile and the reference shear-free CBL buoyancy flux profile and then dividing by the integral of the shear-production term of the TKE balance equation. This procedure is illustrated in Fig. 3. The ZOM integral buoyancy flux for the shear-free CBL, calculated from (3) with $A_R = C_1 = 0.2$, is

$$\int_0^{z_i} B\, dz = 0.4 B_s z_i. \quad (8)$$

If the shear-produced TKE is used for entrainment, the buoyancy flux profile will be shifted to the left as com-
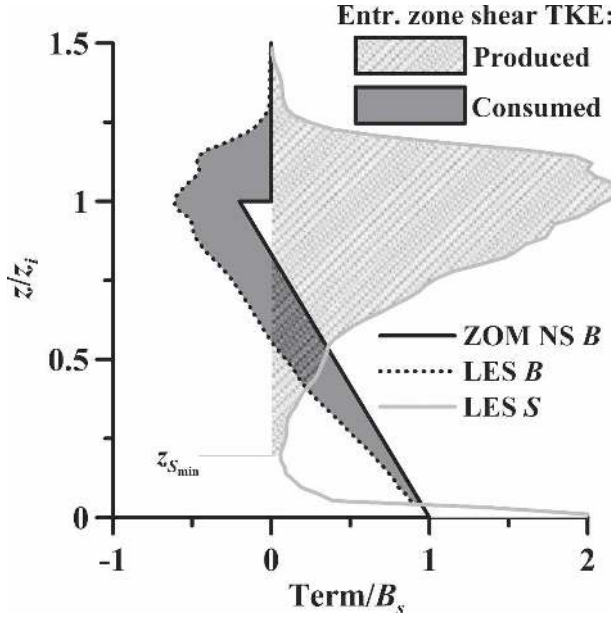
FIG. 3. Illustration of the calculations for evaluating, from the LES output, the fraction of entrainment zone shear-produced TKE that is used for entrainment. The profiles indicate the shear production of turbulence (gray line) and buoyancy production of turbulence (dotted black line) for the GS case (see subsection 3c and Part II) and the reference buoyancy flux for the NS case (solid black line). The hatched area shows the integral entrainment zone shear production of TKE and is evaluated from the minimum above the surface layer to the top of the entrainment zone. The shaded area shows the buoyancy consumption of entrainment zone shear-produced TKE and is evaluated from the surface to the top of the entrainment zone.

pared with the buoyancy flux profile in the shear-free CBL. This leftward shift is shown in Fig. 3 and is also demonstrated in Fig. 8 of Pino et al. (2003). The differences between the sheared and shear-free profiles reflect the contribution of the shear-produced TKE to entrainment. We can therefore integrate the difference over the depth of the CBL to estimate the contribution of shear-generated turbulence to entrainment.

Second, as can also be seen in Fig. 3 and in Fig. 8 of Pino et al. (2003), the shear production of TKE is concentrated in the surface layer and at the top of the CBL with a minimum in shear production at the level $z = z_{S\min}$. This does not have to be true all the time but, for the CBL cases discussed in this paper, such a level almost always exists. The LES results presented below suggest that, consistent with the findings of Lenschow (1970, 1974), Deardorff and Willis (1982), and Moeng and Sullivan (1994), the surface shear-generated TKE [the first two terms in Eq. (7)] is mostly locally dissipated, so it could be neglected in the calculations of integral shear-production of TKE.

We therefore integrate the shear production from

$z = z_{S\min}$ upward to the top of the entrainment zone z_{iu}. Then, the fraction of shear-produced TKE available for entrainment C_P can be defined as the ratio of the integral of the buoyancy flux difference to the integral shear production between $z = z_{S\min}$ and $z = z_{iu}$:

$$C_P = \frac{\displaystyle\int\limits_0^{z_{iu}} B\, dz - 0.4 B_s z_i}{\displaystyle\int\limits_{z_{S\min}}^{z_{iu}} \left(\tau_x \frac{\partial u}{\partial z} + \tau_y \frac{\partial v}{\partial z} \right) dz} . \tag{9}$$

The method used to evaluate particular terms of (9) from LES data is illustrated in Fig. 3. The estimates of C_P derived from LES are presented in section 4g.

d. Selection of parameter space

The choice of parameter space for the background shear in the present study was based on a scale analysis of the ZOM TKE equation (7). Because we are specifically interested in the relative differences between the shear and buoyancy contributions to the TKE budget, we concentrate on the terms of (7) that describe these contributions. Let us adopt values of $z_i = 1000$ m, $u_m = 10$ m s^{-1}, a surface friction velocity of 0.5 m s^{-1}, and $\Delta u = 3$ m s^{-1} as typical for atmospheric conditions. For the CBL entrainment rates and surface temperature flux, we may adopt values from the Fedorovich et al. (2004a) study by taking $dz_i/dt = 0.15$ m s^{-1} and $Q_s = (g/\theta_0)^{-1}B_s = 0.3$ K m s^{-1}, respectively, which are typical for a day with relatively strong sensible heating. This yields an entrainment zone shear term of 0.8 m^3 s^{-3} and a surface shear term of 5 m^3 s^{-3}. For the buoyancy contribution, assuming an entrainment flux ratio of 0.2 (it could actually be larger in sheared CBLs), we come up with the surface buoyancy flux contribution to the integral TKE of 5 m^3 s^{-3} and the entrainment zone buoyancy flux contribution of -1 m^3 s^{-3}. Under such conditions, the shear production of TKE in the entrainment zone is nearly an order of magnitude less than the integral buoyant production of TKE. The surface shear production of TKE is comparable to the buoyancy production at the surface, but much of TKE produced by shear at the surface is known to be locally dissipated (Lenschow 1970, 1974; Deardorff and Willis 1982; Moeng and Sullivan 1994; Part II). The results of this analysis show that it would be desirable to use larger values of shear and/or mixed layer velocity in the LES experiments in order to make the magnitudes of buoyancy and shear contributions comparable. To increase the integral entrainment zone shear production of TKE
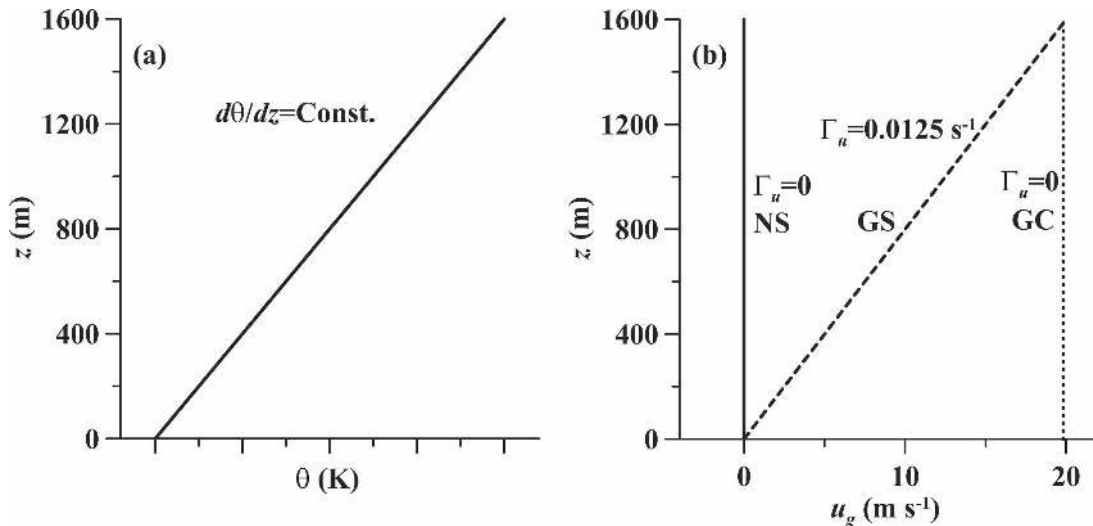
FIG. 4. Initial profiles of (a) the potential temperature θ and (b) the x component of the geostrophic wind velocity, u_g, for the simulated CBL cases. In (b), the solid line represents the NS case simulation, dashed line the GS case simulation, and dotted line the GC case simulation.

to a value comparable to the integral buoyancy production of TKE would require $\Delta u = 10$ m s^{-1}, which would lead to a geostrophic shear stronger than would be typical for the atmosphere. Another option would be to use a weaker surface buoyancy flux to allow the relative effects of shear to stand out more strongly. We have exercised both of these options to some extent, and, as a result, the upper limit of the surface temperature flux used in our study was set to 0.3 K m s^{-1} as in Fedorovich et al. (2004a), and the value of 0.03 K m s^{-1} was adopted as the lower limit in the present study.

The simulation setup for the sheared CBL cases was designed to elucidate the effects of surface shear versus shear across the CBL top. All investigated sheared CBL cases (see below) were divided into a subset that had a constant geostrophic wind (GC), in which all the initial shear was concentrated at the surface, and into a subset of cases in which the surface geostrophic wind was zero; but the shear in the geostrophic wind was strong (GS), so the growing boundary layer would encounter changing wind with height, resulting in concentration of shear at the CBL top. These two cases were compared against a subset of shear-free CBL cases, designated as the NS cases. In all simulated cases, the winds were initialized in geostrophic balance throughout the simulation domain.

In the GS cases, the initial conditions were equivalent barotropic [see Wallace and Hobbs (1977) for a definition of the term equivalent barotropic], with a geostrophic wind starting at 0 m s^{-1} at the surface and increasing to 20 m s^{-1} at a height of 1.6 km (the top of the simulation domain). Although not particularly com-

mon, wind shear of the GS case magnitude is described by Brost et al. (1982a,b) in their analysis of atmospheric CBL data. Despite the fact that such strong shear does not always lie entirely in the geostrophic component of the flow, we chose to use geostrophic shear to keep the free-atmospheric forcing from changing significantly during the simulation.

Thermal wind balance requires such shear to be accompanied by a large-scale temperature gradient. However, in the conducted simulations, such a temperature gradient would only amount to a temperature change of 0.2 K across the entire simulation domain of 5 km, which, in most cases, would provide an insignificant (less than 10%) contribution to the total observed temperature variance in the mixed layer. Because the GS cases are equivalent barotropic, the temperature advection by the geostrophic wind is zero, and the large-scale temperature advection effects have been omitted in the simulations, although such advection may still occur as a result of the ageostrophic component of the flow. Sorbjan (2004) has performed LES studies of baroclinic CBLs in which temperature advection effects can be significant and discussed possible ways to represent them in LES.

For the background free-atmosphere potential temperature stratification, we adopted the range of conditions in Fedorovich et al. (2004a) but with only three gradations of potential temperature stratification: 0.001, 0.003, and 0.010 K m^{-1}. The initial profiles of momentum and buoyancy for the GS and GC cases are shown in Fig. 4.

The array of LES cases is presented in Table 1. The

TABLE 1. Free-atmospheric temperature gradient and surface temperature flux in conducted LES runs for NS: no shear case, GS: geostrophic shear case, and GC: constant geostrophic case.

		Surface temperature flux (K m s^{-1})		
		0.03	0.10	0.30
Potential temperature gradient (K m^{-1})	0.010		NS, GS, GC	NS, GS, GC
	0.003	NS, GS, GC	NS, GS, GC	NS, GS, GC
	0.001	NS, GS, GC	NS, GS, GC	NS, GS, GC

LES code used in this study is described in detail in Fedorovich et al. (2001a) except that the boundary conditions were revised to bring the code into a suitable form for simulating the atmospheric horizontally homogeneous CBL (Fedorovich et al. 2004a). The general settings used in the LES for this study are described in Table 2. The simulations were allowed to proceed until the CBL depth reached approximately 60% of the LES domain depth. At that point, to avoid spurious effects associated with the entrainment zone impinging upon the sponge layer applied in the current version of our LES code, the simulations were stopped.

Output flow statistics were calculated by averaging across horizontal planes. The statistics were calculated every 100 seconds in the simulation, an interval that, in most cases, was much less than the convective overturning time scale in the simulations. This scale is defined as z_i/w_*, where z_i is the CBL depth and w_* is the Deardorff (1970b) convective velocity scale. The calculated flow statistics are listed in Table 3. Because a staggered grid was used, all variables were interpolated to the center of the grid cell, if necessary, before calculating statistics. The dissipation rates were taken directly from their parameterized subgrid values.

e. Definition of CBL depth

For traditional reasons explained in Fedorovich et al. (2004a), the level of the heat flux minimum in the en-

trainment zone was used as the definition of the boundary layer depth z_i. Although the heat flux minimum method results in some undesirable scatter in the estimates of z_i compared with other methods of estimating z_i (Sullivan et al. 1998; Fedorovich et al. 2004a), it appears to provide the definition of the CBL depth that is most consistent with the dynamics of the problem. Because the structure of the upper portion of the entrainment zone changes with time, the altitude of maximum temperature gradient tends to grow more slowly than predicted by the well-established $t^{1/2}$ relationship for the shear-free CBLs discussed in Fedorovich et al. (2004a).

To provide smoother estimates of dz_i/dt, the values of z_i were interpolated between the discrete LES grid levels by using a quadratic fit at the grid minimum level and the surrounding two levels. The lower limit of the entrainment zone z_{il} was defined as the zero-crossing height of the buoyancy flux profile, using linear interpolation between discrete grid points. Following Fedorovich et al. (2004a), the point at which the buoyancy flux returned 90% of the way back to zero from its grid minimum was used as the definition of the upper limit of the entrainment zone z_{iu}.

4. Results and discussion

Simulation results shown in this section are arranged on the nine-panel figures according to the surface tem-

TABLE 2. Parameters of conducted LES.

Parameter	Setting
Domain size	5.12 × 5.12 × 1.6 km^3
Grid	256 × 256 × 80
Surface kinematic temperature flux	0.03, 0.1, and 0.3 K m s^{-1}
Potential temperature stratification above CBL	0.001, 0.003, and 0.010 K m^{-1}
Geostrophic wind	0 m s^{-1} throughout domain (NS)
	20 m s^{-1} throughout domain (GC)
	0 m s^{-1} at lower boundary, 20 m s^{-1} at top (GS)
Time step	0.5 s (to synchronize NS, GS, and GC cases)
Lateral boundary conditions	Periodic for all prognostic variables and pressure
Upper boundary conditions	Neumann with zero gradient, a sponge layer imposed in the upper 20% of simulation domain
Lower boundary conditions	No-slip for velocity, Neumann for temperature, pressure, and subgrid TKE, Monin–Obukhov similarity functions as in Fedorovich et al. (2001a)
Subgrid turbulence closure	Subgrid TKE-based after Deardorff (1980)

TABLE 3. Statistics calculated in LES.

Statistics category	Quantities calculated
First order	$\overline{u}, \overline{v}, \overline{\theta}, \overline{E}$ (subgrid energy), ε**
Second order*	$\overline{u'^2}, \overline{v'^2}, \overline{w'^2}, \overline{\theta'^2}, \overline{E'^2}, \overline{w'\theta'}, \overline{w'u'}, \overline{w'v'},$ $\overline{w'e'}$**, $\overline{w'p'}$**
Third order	$\overline{w'w'w'}, \overline{\theta'\theta'\theta'}$
Spectra	$\overline{u'^2}, \overline{v'^2}, \overline{w'^2}, \overline{\theta'^2}$
Cospectra	$\overline{w'\theta'}, \overline{w'u'}, \overline{w'v'}$

* For the statistics $\overline{u'^2}$, $\overline{v'^2}$, $\overline{w'^2}$, $\overline{w'\theta'}$, $\overline{w'u'}$, and $\overline{w'v'}$, both resolved and total (resolved plus subgrid) components were calculated. Overbars represent horizontal averages in LES, which are intended to be representative of ensemble averages.

** Not available for all cases.

perature flux and the free atmospheric stratification, with surface temperature flux increasing from left to right and potential temperature stratification increasing from bottom to top. Wherever time forms the abscissas of the plots, the x axes in the plots are stretched or compressed to allow the simulation to span the available space in the plot and to highlight the differences between the NS, GS, and GC cases.

a. CBL growth and momentum profiles

The enhancement of CBL growth in the presence of shear (Fig. 5) appears to be qualitatively consistent with the results of the scale analysis performed in section 3d. In the right-hand-column plots (Figs. 5c,f,i), the TKE production is dominated by the strong surface buoyancy flux, and in those cases the evolution of the sheared CBLs does not considerably differ from that of the NS CBLs. In the left-hand-column plots (Figs. 5d and 5g), however, the sheared CBLs grow significantly faster than the NS CBLs. In those cases, the surface buoyancy flux is weakest, allowing the effects of shear-generated turbulence to be seen more clearly. Two additional features of CBL evolution can be noticed through more careful examination of Fig. 5: 1) the free-atmosphere potential temperature stratification appears to modulate the sheared CBL evolution and 2) the relationship between the GS and GC cases is rather variable among the simulated cases.

Although the rate of CBL growth is directly related to the strength of the surface buoyancy flux, there are some secondary effects of the boundary layer growth rate in sheared CBLs that cannot be tied directly to the surface buoyancy flux. If the CBL growth rate becomes sufficiently large, the active entrainment of momentum prevents turbulence from mixing the velocity field in the CBL interior [see Fig. 6, a similar effect has been noted in atmospheric CBL data by LeMone et al. (1999)]. As a result, if the momentum is not well mixed

in the CBL interior, shear does not accumulate at the CBL top, preventing the shear-generated turbulence from significantly contributing to the entrainment and, through it, to the CBL growth. This feature may be interpreted as a negative feedback mechanism relating the CBL growth rate and the accumulation of shear at the CBL top, the understanding of which requires some additional analysis that is presented in section 4b. As can be seen in Figs. 5f,h,i, the sheared CBLs presented there do not grow more quickly than the NS CBLs, while the velocity profiles in Figs. 6f,h,i show the least concentration of shear in the entrainment zone.

These secondary effects of CBL growth rate are further seen by comparing Figs. 5e and 5h. The CBL cases shown there have the same surface buoyancy flux, but the sheared CBLs relative to the NS case grow faster in Fig. 5e than in Fig. 5h, even though the free atmospheric stratification is weaker in Fig. 5h (which should make it easier for shear-generated turbulence to develop).

Based on these results, one may infer that in CBLs, which grow in a more stably stratified atmosphere, more shear accumulates at the CBL top and, therefore, more shear enhancement of entrainment is observed. However, when the stratification becomes sufficiently strong, its turbulence-suppressing effects outweigh the effects of the accumulated shear, as can be seen by comparing the CBL growth rates for the GS cases shown in Fig. 5b versus those in Fig. 5e, and in Fig. 5d versus Fig. 5g. In those cases, shear-generated turbulence more strongly enhances the entrainment when the background stratification is weaker.

The effects of stratification may be better seen by comparing CBLs with similar rates of growth (Figs. 5c,e,g and Figs. 6c,e,g). Those in more weakly stratified environments have more pronounced shear-enhanced growth than do those growing in more strongly stratified environments, although one must keep in mind that the buoyancy flux is the dominant contributor to the TKE production in CBLs shown in the upper right panels. Nevertheless, we can observe that the turbulence, enhanced by shear, is mixing the momentum more actively in the entrainment zones of the CBLs with the weakest outer stratifications, implying a balance that exists between the buoyancy and shear production of TKE in the entrainment zone.

As one may conclude from an overall comparison of the considered figures, in the GS cases, which feature background shear, greater shear accumulation takes place at the CBL top, and the GS CBL growth is generally faster than the GC CBL growth. This relationship between the entrainment rates of GS and GC cases is not always the same, however. In Fig. 5b, the growth
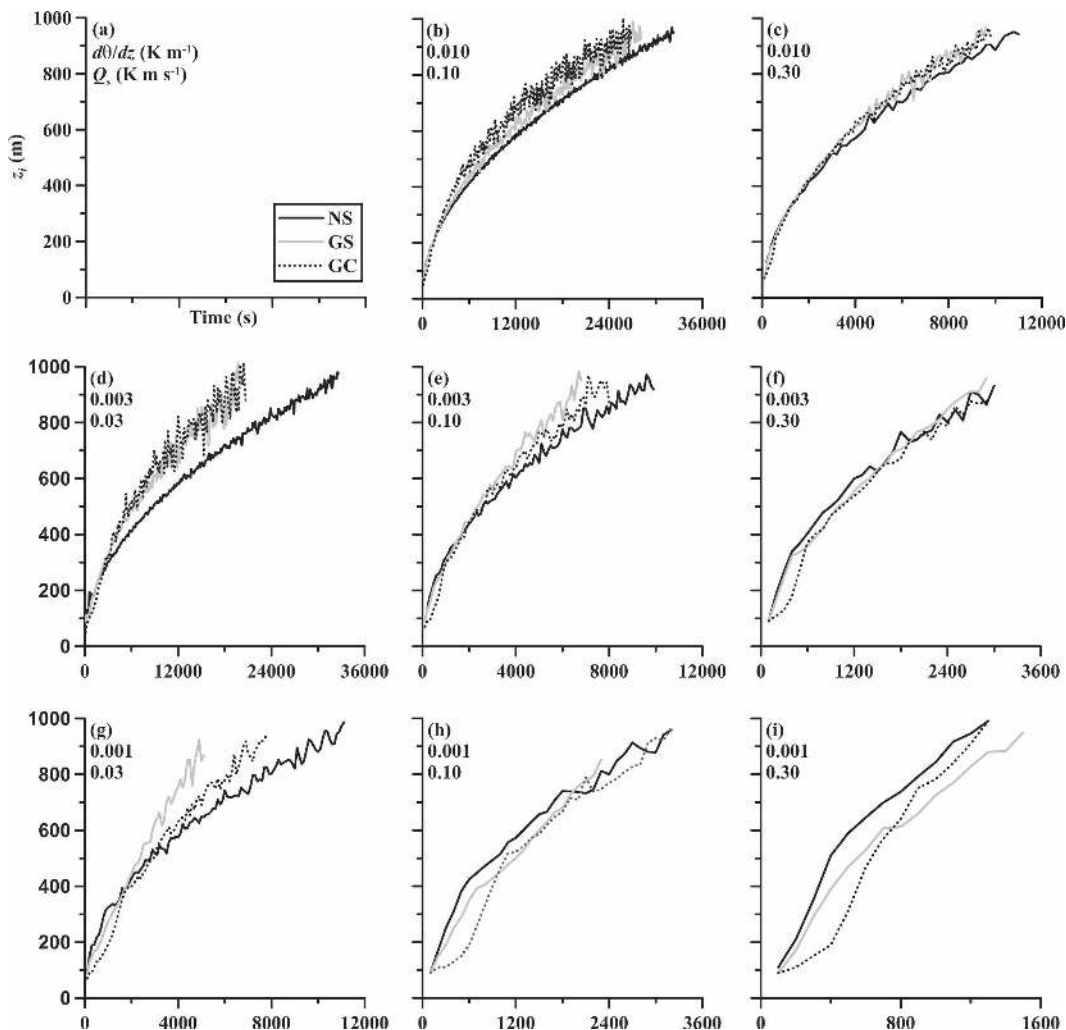
FIG. 5. CBL depth, z_i (m), as a function of time (s) for the LES cases simulated: (a) legend, (b)–(i) simulation results. The potential temperature lapse rate $\partial\theta/\partial z$ (K m^{-1}) and the surface temperature flux Q_s (K m s^{-1}) are indicated in the upper left corner of each plot. Solid black lines denote the NS case simulation results, solid gray lines the GS case results, and dotted black lines the GC case results.

of the GC case CBL outpaces that of the GS case CBL, highlighting one very important finding regarding the behavior of the simulated GC case CBLs. In these CBLs, initially only the surface shear is present, but as the GC case CBL evolves, the surface drag leads to the decrease of velocity throughout the whole depth of the CBL, resulting in the development of shear across the entrainment zone. To some degree, this is true in all the GC cases, as Fig. 6 shows, but when the CBL growth rate is smaller, the effects of surface drag become especially noticeable. In the GC cases shown in Figs. 6f,h,i, velocity in the CBL interior is not much smaller than the free atmospheric velocity due to the rapid entrainment in those cases. In Figs. 6b and 6d, on the other hand, the mixed layer velocity is several meters

per second smaller than the free atmosphere velocity. As a result, the GC case entrainment-zone shear (Figs. 6b and 6d) looks similar to the entrainment-zone shear of the corresponding GS cases. The above observations strongly suggest that (i) the entrainment zone shear plays a more direct role in enhancing CBL growth as compared to the surface shear and (ii) that the effects of surface shear on the CBL growth are only felt indirectly through the reduction of the mixed layer velocity and resulting increase of shear at the CBL top.

The relationship between the growth rates of sheared and shear-free CBLs appears to be essentially reversed in the cases shown in Fig. 5i (and to some extent in the early stages of the simulations demonstrated in Figs. 5f and 5h as well), where the overall growth rate of the
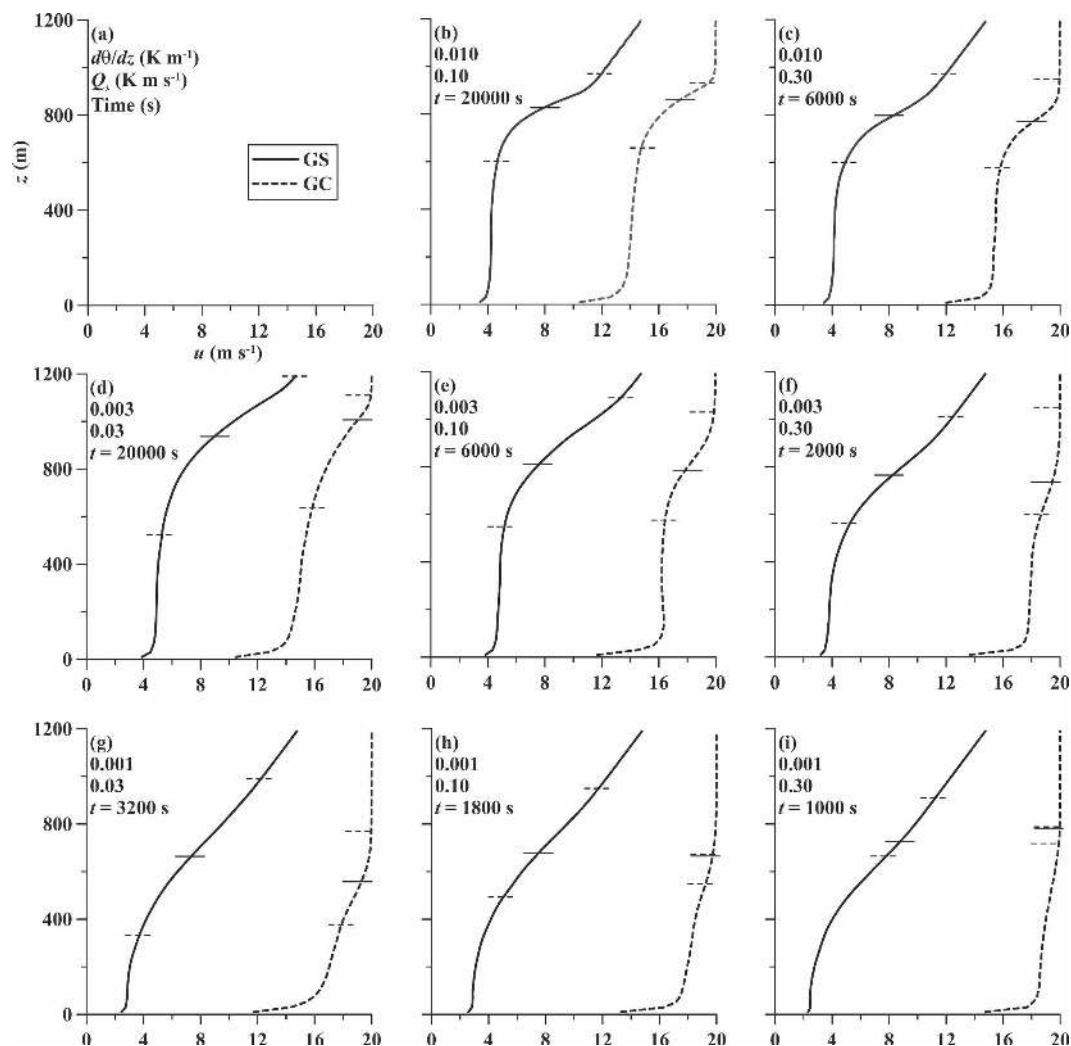
FIG. 6. Profiles of the x component of momentum at selected times during the simulation: (a) legend, (b)–(i) simulation results. The potential temperature lapse rate $\partial\theta/\partial z$ (K m^{-1}), the surface temperature flux Q_s (K m s^{-1}), and the simulated elapsed time (s) are indicated in the upper left corner of each plot. The solid lines represent the profiles from the GS case simulations, and the dashed lines are from the GC case simulations. The CBL depth z_i is marked by a solid line on each profile, and the lower and upper limits of the entrainment zone are indicated by dashed lines.

sheared CBLs is actually lower than the growth rate of the NS CBL. One might regard this as evidence supporting the Hunt and Durbin (1999) theory of shear sheltering of turbulence. However, it should be taken into account that the duration of the simulation in Fig. 5i is rather short so that the CBL evolution and structure are dominated by the onset of resolved turbulence in those simulations, and the turbulence cannot be considered fully developed.

In the GS cases shown in Figs. 5g,h,i, the gradient Richardson number, Ri$_g$ (see section 4f), in the free atmosphere above CBL is only 0.21, a value smaller than the critical value of Ri$_g$ = 0.25 for the onset of

Kelvin–Helmholtz instability in continuously stratified laminar flows (Kundu 1990). This critical Ri$_g$ value is a necessary but not sufficient condition for the onset of KH instability but, nevertheless, the stability of the free-atmosphere flow, just above the CBL, to finite perturbations cannot be guaranteed in these cases. In Figs. 5h and 5i, the duration of the simulations is probably too short to allow the instability to be clearly seen, but the profiles in Fig. 5g may reflect some vertical mixing caused by instability.

The cases with $\partial\theta/\partial z = 0.003$ K m^{-1} and $Q_s = 0.03$ K m s^{-1} (shown in Figs. 5d and 6d) were chosen for more detailed analysis in sections 4d through 4f below, as
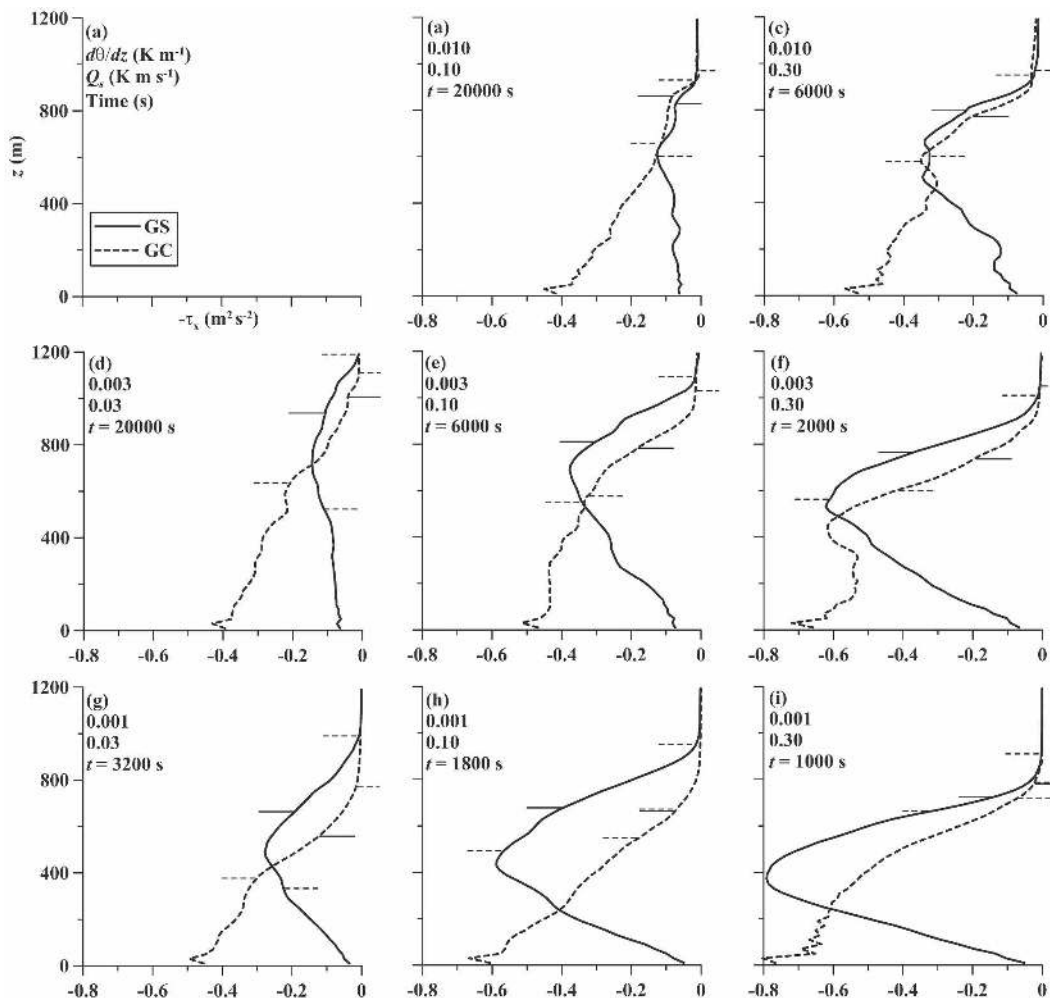
FIG. 7. Profiles of the *x* component of momentum flux at selected times during the simulation: (a) legend, (b)–(i) simulation results. For notation, see Fig. 3.

well as in Part II, because they meet three important criteria: 1) the effects of shear on CBL evolution are relatively strong; 2) the GC CBL and the GS CBL experience a similarly large growth rate (actually, in the early stage of the simulation, GC CBL grows a little faster); and 3) the background atmosphere is guaranteed to be stable in the KH sense.

b. Momentum flux profiles

To understand the relationship between the velocity profiles and the CBL growth rate discussed above, we take a look at the vertical turbulent fluxes of the horizontal momentum components normalized by density: $-\tau_x = \overline{w'u'}$ and $-\tau_y = \overline{w'v'}$. The flux of velocity is commonly, although inaccurately, called the momentum flux, and for the sake of convenience we will adopt this nonprecise terminology in our further discussion.

Figure 7 illustrates the *x* component of momentum

flux, showing that turbulent entrainment of momentum is strongest in the most rapidly growing CBLs (Figs. 7f,h,i); yet the momentum fields in those CBLs are not well mixed (Fig. 6). As noted above, in these cases the turbulent mixing is obviously insufficient to evenly distribute the rapidly entrained momentum within the CBL.

We can borrow, at this point, the ZOM representation of the CBL structure (Fig. 1) in order to understand these relationships among the CBL growth, momentum flux, and velocity profiles. This representation is extremely idealized, and the LES and atmospheric profiles do not always adhere to such an ideal structure. However, a simple analysis in this case can yield insight into the competing processes that shape the CBL momentum profile. In order for the mixed layer velocity to be constant with height (well mixed) as it is in the ZOM (see Fig. 1), we would expect the momentum flux to be

linear throughout the mixed layer (Fedorovich 1995) and drop sharply to zero at z_i (in the ZOM, it has a discontinuity at z_i). In the GS case CBL, the flux magnitude would be zero just above z_i, jump down to some negative value just below z_i, and then increase linearly toward the lower surface. In order for these conditions to be met, the momentum flux at the CBL top must match the product of the velocity jump and the CBL growth rate,

$$-\tau_x(z_i) = -\Delta u \frac{dz_i}{dt}, \tag{10}$$

as it is expressed in the ZOM. By retrieving Δu and dz_i/dt consistently with their definitions in the ZOM (see Fig. 1), we find that $-\Delta u dz_i/dt = -0.43$ m^2 s^{-2} for the GS case CBL in Fig. 7e and $-\Delta u dz_i/dt = -2.5$ m^2 s^{-2} for the GS case CBL in Fig. 7i. Looking at the actual momentum flux profiles, we see in Fig. 7e a minimum of -0.4 m^2 s^{-2}, which is about what we might expect from Eq. (10), but the minimum of -0.8 m^2 s^{-2} in Fig. 7i is much weaker than expected. The momentum flux is therefore outpaced by the CBL growth, and the velocity field remains rather unmixed as may be concluded from Fig. 6i.

The ability of the momentum-mixing effects of turbulence in the CBL interior to keep pace with the entrainment of momentum at the CBL top can be further conceptualized by comparing the velocity scales associated with both. Near the end of the simulations in Figs. 7f,h,i, the CBL growth rate (0.3 to 0.5 m s^{-1}) approaches a range of values comparable with the Deardorff (1970b) convective velocity scale (1.5 to 2 m s^{-1}), and the mean shear in the CBL interior is still rather noticeable. On the other hand, in the well-mixed CBL cases (Figs. 6b,c,d), the growth rate (0.02 to 0.05 m s^{-1}) is nearly two orders of magnitude less than the convective velocity scale (1 to 2 m s^{-1}), indicating the dominance of mixing effects of the turbulence in the CBL interior relative to the entrainment of momentum. As was discussed in Fedorovich et al. (2004b), the scaled TKE is generally lower in CBLs growing under conditions of weaker outer stratification, so there is slightly less turbulence available in these cases to mix the momentum.

Other than these competing effects of momentum entrainment at the CBL top and mixing in the CBL interior, the displayed momentum flux profiles are reflective of the different initial velocity profiles representative of the GC and the GS cases. The GC case momentum flux profile is typically characterized by a minimum near the surface, with the flux slowly increasing throughout much of the CBL interior (positive vertical flux divergence $-\partial\tau_x/\partial z$), and then increasing more rapidly to zero in the upper portion of the CBL (stronger flux divergence and strong entrainment of momentum). The GS case CBLs feature negative flux divergences $-\partial\tau_x/\partial z$ in their lower portions, indicating an acceleration of the flow by the turbulence—a somewhat less typical feature of the CBL structure. What is most important is that in the GC case profiles, the flux divergence in the CBL interior shows the effects of surface friction spreading through the entire CBL interior, illustrating how the momentum fluxes contribute to the accumulation of shear at the CBL top.

c. Entrainment flux ratio

As might be expected, the sheared CBLs demonstrate larger values of the entrainment heat flux ratio A_R. Note that the NS case CBLs consistently have $A_R \approx 0.2$. The behavior of A_R retrieved from LES, in general, is consistent with most of the other findings presented in sections 4a and 4b. Provided the CBL growth is slow enough to allow accumulation of shear at the CBL top, the sheared CBL entrainment flux ratios are larger under conditions of weaker free-atmosphere stratification, as was observed for the entrainment rates in Fig. 5. In particular, the comparison of the plots in Figs. 8b,d,g indicates that the ratios become largest in the GS case CBL where the background potential temperature stratification is too weak to sufficiently suppress turbulence (Fig. 8g). The ratios A_R are considerably smaller in Fig. 8b, corresponding to the case of much stronger background stratification.

Additionally, the negative feedback between the entrainment of momentum and the CBL growth, discussed above (see section 4a), is reflected in the entrainment flux ratios presented in Figs. 8e and 8h. Although the GS case CBL in Fig. 8h has weaker background stratification than in Fig. 8e, its entrainment flux ratios are smaller than that in the CBL case shown in Fig. 8e.

More importantly, the differences in behavior between the GC and GS cases are seen in the A_R values. In the GS cases, A_R starts out rather small because entrainment zone shear is initially weak. However, once the CBL becomes more developed, the shear increases, and the entrainment flux ratio increases throughout the remainder of the simulation (Figs. 8d,e,g). The growth in A_R does seem to be limited when the outer stratification is stronger and, in some cases (Figs. 8b and 8c), it approaches a nearly constant value that only slightly exceeds its NS value.

In the GC cases, A_R increases very rapidly with the onset of turbulence at the beginning of the simulation and then decreases slowly or remains approximately
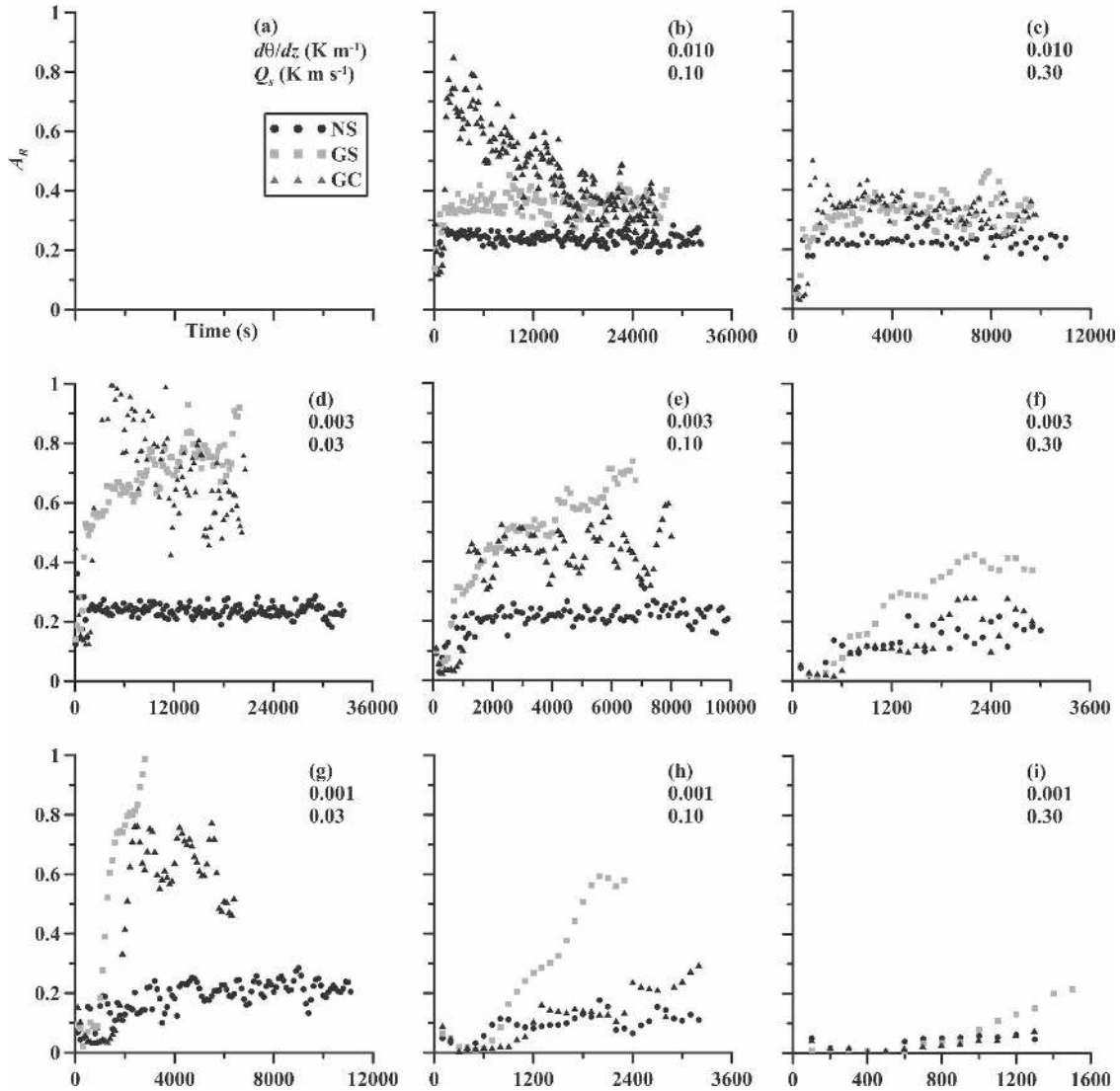
FIG. 8. Time series of the entrainment flux ratio A_R: (a) legend, (b)–(i) simulation results. The potential temperature lapse rate $\partial\theta/\partial z$ (K m^{-1}) and the surface temperature flux Q_s (K m s^{-1}) are indicated in the upper right corner of each plot. Solid black circles show the NS case simulation data, gray squares the GS case data, and solid black triangles the GC case data.

constant thereafter. The characteristics of the initial jump of A_R are related to the onset of turbulence, which is largely dependent on the method of initialization and the numerical scheme used, so the initial jump A_R in the simulations may not perfectly reflect its behavior in the atmosphere. Nevertheless, the gradual decrease of the entrainment flux ratio with time in the GC case simulations (Figs. 8b and 8d) is smooth and long enough for the CBL to forget about these early stages of development, so the results on A_R at the later stages of the CBL development generally look trustworthy.

One may think of two reasons for the initial jump in A_R in the GC cases. In the initial stage of its develop-

ment, the CBL may be so shallow that the effects of surface drag are felt very strongly, and velocity in the CBL interior decreases in time very rapidly. In such a case, strong entrainment-zone shear would appear relatively early in the simulations, and the resulting shear-generated TKE would cause strong entrainment at the onset of resolved turbulence. Alternatively, the proximity of the entrainment zone to the surface layer during these early stages may make it easier for the surface shear-generated TKE to be transported to the entrainment zone where it can contribute to the entrainment. This may explain some of the entrainment behavior seen in Figs. 8b and 8d, where the entrainment flux
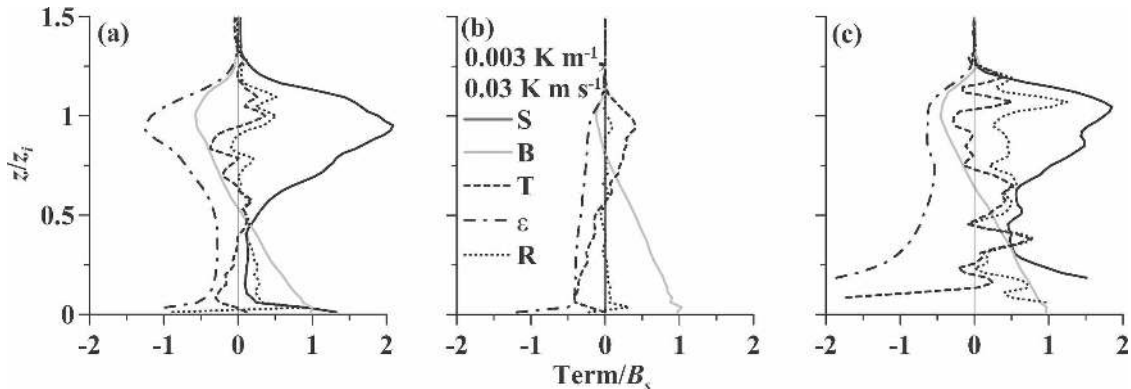
FIG. 9. Components of the TKE budget from the LES runs with stratification of $\partial\theta/\partial z = 0.003$ K m^{-1} and a surface heat flux of $Q_s = 0.03$ K m s^{-1} for (a) GS, (b) NS, and (c) GC cases. The solid black lines denote the shear production terms, solid gray lines the buoyancy terms, dashed black lines the vertical transport term, dot–dashed black lines the dissipation, and dotted black lines the residual. The profiles are shown for the time in the simulation when the CBL depth z_i was approximately 800 m.

ratio slowly decreases with time. This decrease is not observed in all cases (see, e.g., Fig. 8e). A look at the TKE budgets and their evolution might help to determine which of these two mechanisms is the primary contributor to entrainment in the GC case CBLs.

d. TKE budgets

For reasons explained in section 4a, we focus in our analyses on the cases with $\partial\theta/\partial z = 0.003$ K m^{-1} and $Q_s = 0.03$ K m s^{-1}. The TKE budgets were calculated at moments when the CBL depth in all cases was close to 800 m so that the resolution of the CBL structure was the same.

In general, the budgets have may of the same characteristics shown in Fig. 11 of Moeng and Sullivan (1994) and Fig. 7 in Pino et al. (2003), and the effects of shear stand out quite vividly in the entrainment zone (Figs. 9a and 9c). The heat flux minimum is larger and the entrainment zone is considerably deeper in both the sheared CBLs than in the shear-free CBL. The shear production terms in the entrainment zone are of comparable magnitude in the GS and GC cases.

The dissipation of TKE in the entrainment zone of sheared CBLs (Figs. 9a and 9c) is enhanced relative to the NS case (Fig. 9b). In fact, the dissipated fraction of TKE appears to be larger than suggested by Price et al. (1978), who found that roughly 30% of the shear-generated TKE is subject to the dissipation. This result necessitates further investigation into the fraction of entrainment zone shear-generated TKE that is used for entrainment (see section 4g).

The TKE transport term seems to indicate that the surface shear-generated TKE is not being transported from the surface layer into the entrainment zone. In the

GC case CBL, the TKE upward transport near the surface is enhanced, but the dissipation term is also very large there. In the middle of the CBL, the transport term does not differ much from its NS case counterpart, suggesting nearly all the surface shear-generated TKE is dissipated in the lower CBL. In the entrainment zone, the transport term is smaller in the GC case than it is in the NS case. Given that the GS case transport is similarly small in the entrainment zone while the GS case shear production is similarly large, this suggests that the upward transport of buoyancy-generated TKE is simply offset by the downward transport of entrainment zone shear-generated TKE and that the upward transport of surface shear-generated TKE is not making a significant contribution to the TKE in the entrainment zone. Nevertheless, it should be taken into account that the TKE budgets displayed in Fig. 9 are taken rather late in the simulation when the entrainment zone is more distant from the surface layer.

e. Evolution of the velocity and TKE budget profiles

At earlier stages in the simulations, the TKE budget and velocity profiles likewise show the entrainment zone shear to be making the bulk of the contribution to the enhanced entrainment in the GC cases. In the velocity profiles (Figs. 10a and 10b), the value of u in the interior of the CBL decreases very quickly early in the simulation, and the entrainment zone shear is immediately large when the CBL becomes established. The overall jump in u across the entrainment zone then changes very little between $t = 2500$ s and $t = 20\,000$ s, maintaining a value of about 4 m s^{-1}. Meanwhile, the v profiles show a substantial increase in the v jump across
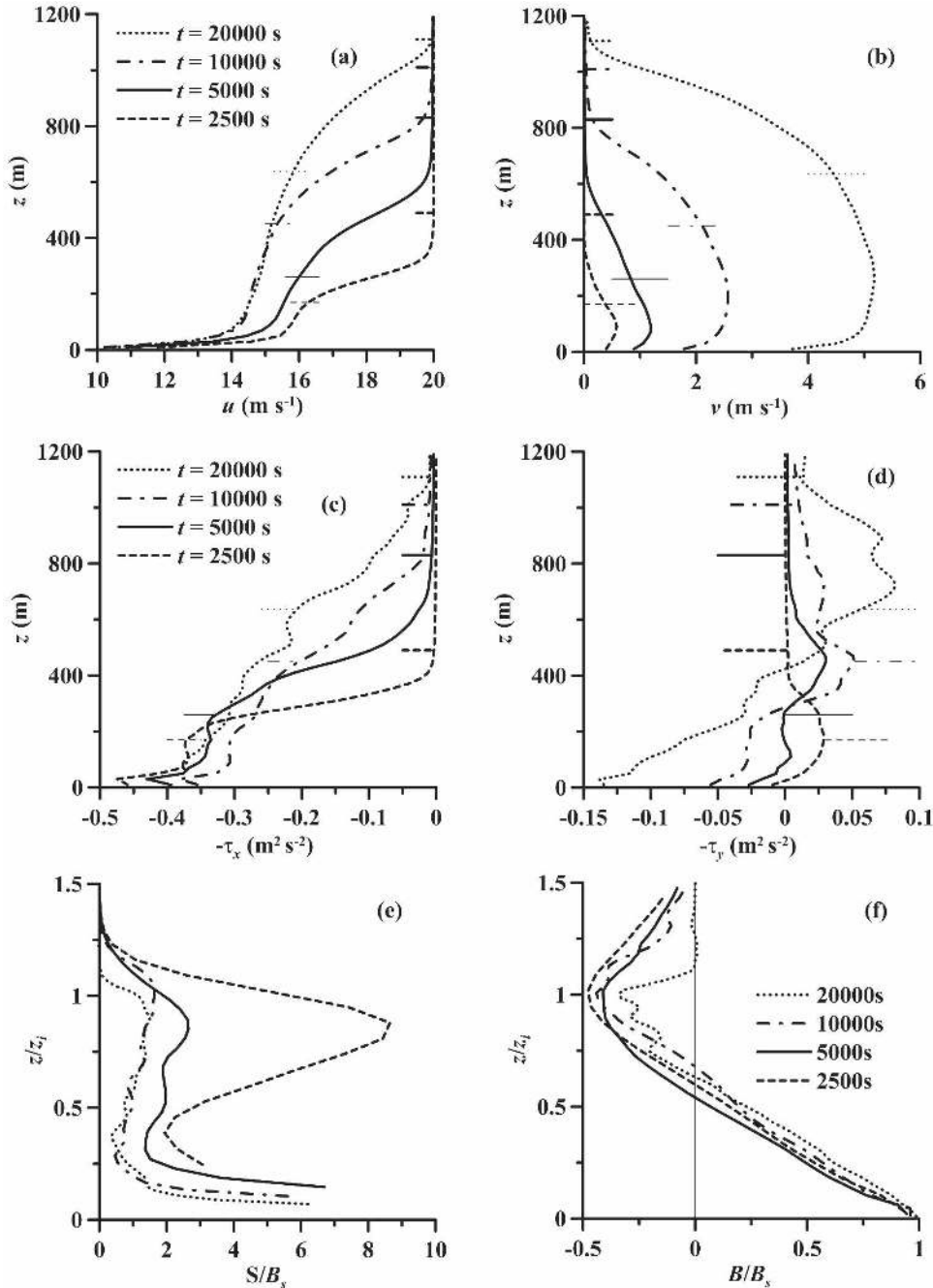
FIG. 10. Evolution of the mean wind, vertical momentum flux, and TKE budget profiles for the GC case CBL with $\partial\theta/\partial z = 0.003$ K m^{-1} and $Q_s = 0.03$ K m s^{-1}: (a) x component mean wind, (b) y component mean wind, (c) x component momentum flux, (d) y component momentum flux, (e) shear production of TKE, and (f) buoyancy production of TKE. The lower and upper limits of the entrainment zone (defined as the region of negative heat flux) are marked by thin and thick horizontal lines, respectively. The profiles are from the following elapsed times in the simulation: 2500 s (dashed lines), 5000 s (solid lines), 10 000 s (dot–dashed lines), and 20 000 s (dotted lines).

the entrainment zone as the simulation proceeds, increasing to over 4 m s^{-1} late in the simulation, so the magnitude of the velocity jump vector increases approximately 50%, from roughly 4 m s^{-1} at $t = 2500$ s

to about 6 m s^{-1} at $t = 20\,000$ s. Since the ZOM-parameterized shear production is proportional to the square of this velocity jump [see Eq. (7)], the shear production can be considered doubled, based on the

velocity jump alone. However, dz_i/dt decreases by more than a factor of 4 (from 0.09 to 0.02 m s^{-1}), so the shear contribution to the integral TKE budget [see Eq. (7)] is cut in half.

Figures 10c and 10d show the evolution of the vertical momentum flux profiles. It is easy to notice that, first of all, the flux of u is a fair bit stronger than the flux of v (the profiles are plotted with different x axes to illustrate the evolution of the profiles). The fluxes exhibit a substantial change across the entrainment zone, approaching zero near the top of the entrainment zone, as turbulence diminishes. In general, the magnitude of the flux in the entrainment zone shows a gradual decrease with time. At $t = 2500$ s, the flux is -0.37 m^2 s^{-2} at the bottom of the entrainment zone, while at $t = 20\,000$ s, it is about -0.21 m^2 s^{-2}. The v-flux magnitudes in the entrainment zone increase a bit over the same time interval, but not enough to compensate for the decrease in the magnitude of $-\tau_x$. The decreasing momentum fluxes are directly related to the decreasing CBL growth rate dz_i/dt during the simulations.

The decreasing momentum entrainment leads to a weaker shear production of turbulence as shown in Fig. 10e. The profiles are plotted in z_i-normalized vertical coordinates in order to show the location of the production relative to z_i. The surface shear generation of TKE, which does not change considerably during the simulation, is truncated in order to highlight the TKE production by entrainment-zone shear. The decrease in shear production with time in the entrainment zone is rather obvious. The buoyancy consumption of TKE in the entrainment zone also decreases with time (Fig. 10f), but not in such a dramatic fashion.

At no stage of the simulation do any of the TKE transport profiles indicate enhanced transport from the surface into the entrainment zone. In fact, the profiles (not shown) all look similar to those in Fig. 9. Based on such behavior, one can conclude that the evolution of the entrainment flux ratio in the GC case is most directly tied to the entrainment-zone shear, not to the upward transport of surface shear-generated TKE.

In the GS case CBL, the net change of u across the entrainment zone increases dramatically during the simulation, climbing from 3.5 m s^{-1} at $t = 2500$ s to 9 m s^{-1} at $t = 20\,000$ s (Fig. 11a). The v profile (Fig. 11b) also contains some increasing shear. The corresponding momentum-flux profiles (Figs. 11c and 11d) show that the x component flux dominates, and its magnitude increases throughout the simulation as the growing CBL encounters ever-greater momentum at its top.

Not surprisingly, Fig. 11e testifies that the shear generation of TKE increases during the simulation as long as the shear magnitude at the CBL top increases. Correspondingly, the buoyancy consumption of TKE (Fig. 11f) increases during the GS case simulation.

This means that the entrainment flux ratio in both the GS and GC case CBLs appears to be directly related to the shear across the entrainment zone. In the GS case CBLs, the entrainment-zone shear is initially zero and it increases during the simulation and, when accompanied by increasing momentum flux, results in greater shear generation of TKE and a corresponding increase in the entrainment-flux ratio. In contrast, the GC case entrainment-zone shear appears as soon as the CBL becomes established and, as its momentum flux decreases due to the slowing CBL growth, the entrainment-zone shear production of turbulence also decreases, resulting in a smaller entrainment flux ratio with time. The analysis clearly shows that, in the GC case, it is the shear production of TKE resulting from entrainment zone shear, not the upward transport of surface shear-generated TKE, which drives the enhanced entrainment.

f. Richardson numbers

Motivated by the discussion in Mahrt and Lenschow (1976) and the results of Kim et al. (2003) and Sorbjan (2004), we investigated the behavior of the gradient and flux Richardson numbers in our simulations. The gradient Richardson number used in Kim et al. (2003) is given by

$$\mathrm{Ri}_g = \frac{N^2}{(\partial u/\partial z)^2 + (\partial v/\partial z)^2}, \qquad (11)$$

where N, $\partial u/\partial z$, and $\partial v/\partial z$ are evaluated locally in z. Additionally, we used in our analyses the flux Richardson number defined as

$$\mathrm{Ri}_f = \frac{B}{\tau_x \partial u/\partial z + \tau_y \partial v/\partial z}, \qquad (12)$$

which represents the ratio of buoyancy production/consumption of turbulence to the shear production of turbulence in the TKE balance.

A Ri_g analysis can be done individually at each grid point to understand the local generation of KH type instabilities. If one adopts an analogy between the stable boundary layer and the entrainment zone atop a sheared CBL (Otte and Wyngaard 2001) and keeps in mind that nocturnal boundary layer turbulence is intermittent in nature, a local Ri_g analysis might reveal particularly useful diagnostic information about the dynamics of turbulence at the top of the sheared CBL. However, such an analysis is complicated by uncertainties in identifying the CBL top locally, especially in locations where the interface is diffuse.
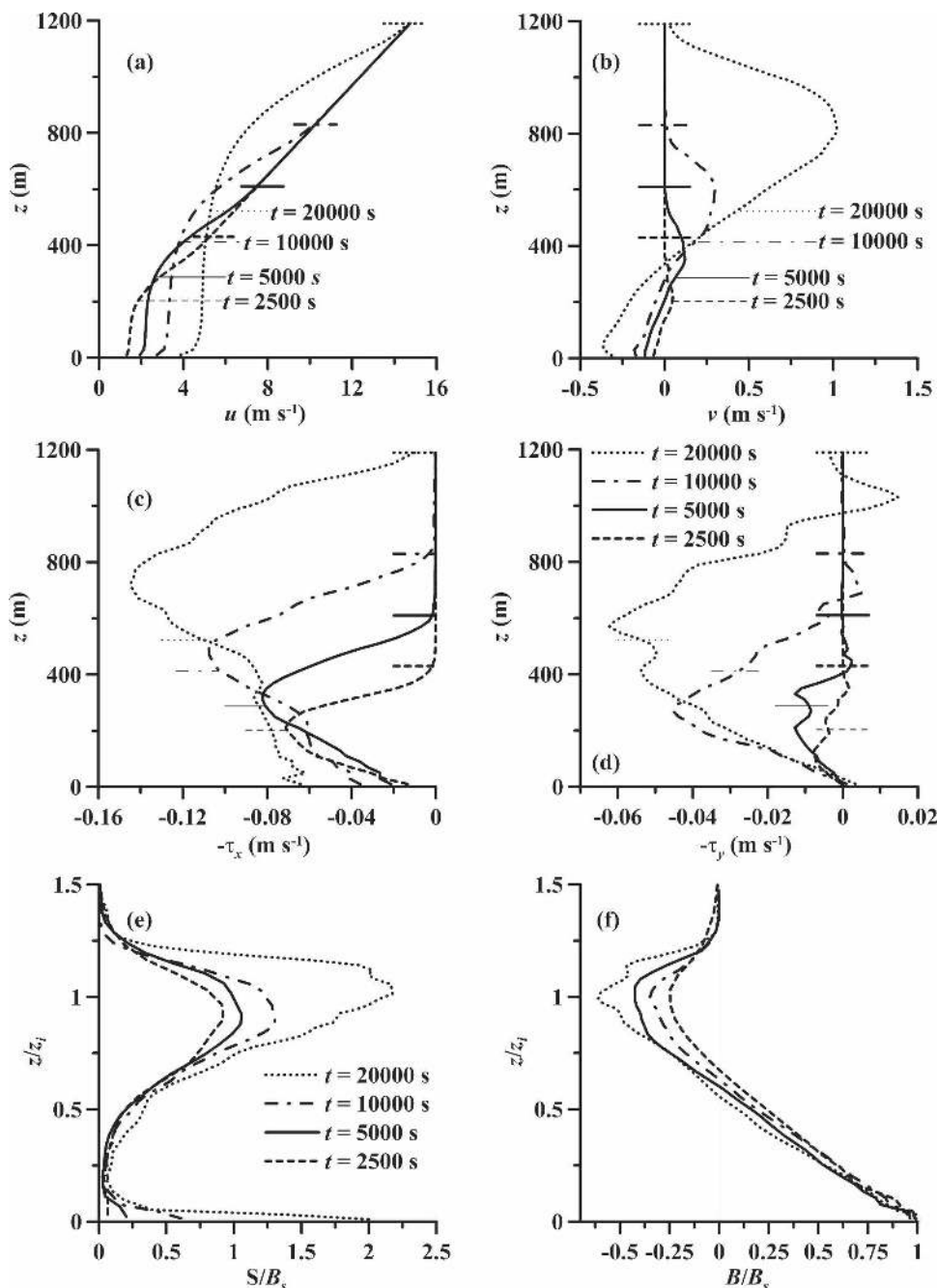
FIG. 11. Evolution of the mean wind, vertical momentum flux, and TKE budget profiles for the GS case CBL having $\partial\theta/\partial z = 0.003$ K m^{-1} and $Q_s = 0.03$ K m s^{-1}: (a) x component mean wind, (b) y component mean wind, (c) x component momentum flux, (d) y component momentum flux, (e) shear production of TKE, and (f) buoyancy production of TKE. For notation, see Fig. 10.

It is much more feasible to evaluate Ri_g from the horizontally averaged profiles. Although the horizontal averaging masks areas where Ri_g is locally small, a small value of average flow Ri_g should point to KH instabilities occupying a considerable area.

We apply our Ri number analyses at $t = 15\ 000$ s for

the GC and GS case CBLs. The Ri profiles for these cases are demonstrated in Figs. 12 and 13, respectively. We also show in these plots the corresponding profiles of u and θ in order to highlight the relationships among shear, temperature gradient, and Ri. Additionally, the profiles of the buoyancy flux B are shown in order to
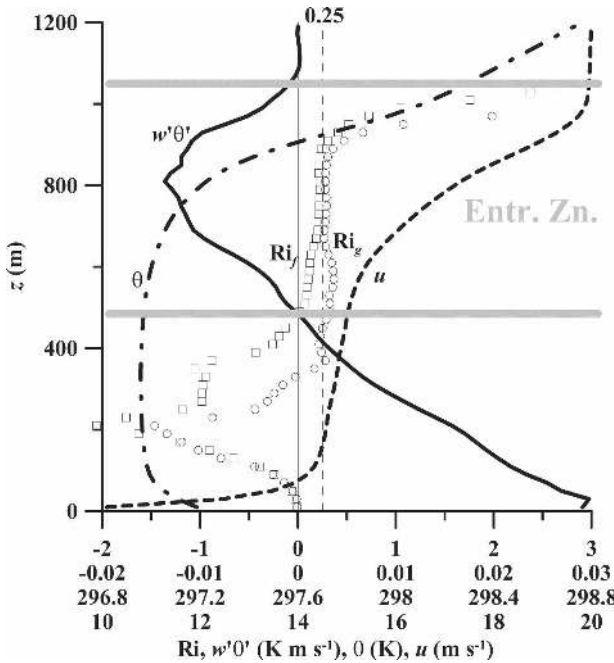
FIG. 12. Profiles of gradient Richardson number Ri_g (open circles), flux Richardson number Ri_f (open squares), potential temperature flux (solid black line), potential temperature (dot–dashed line), and the x component of momentum (dashed line) at $t = 15\,000$ s in the GC simulation with $\partial\theta/\partial z = 0.003$ K m^{-1} and $Q_s = 0.03$ K m s^{-1}.

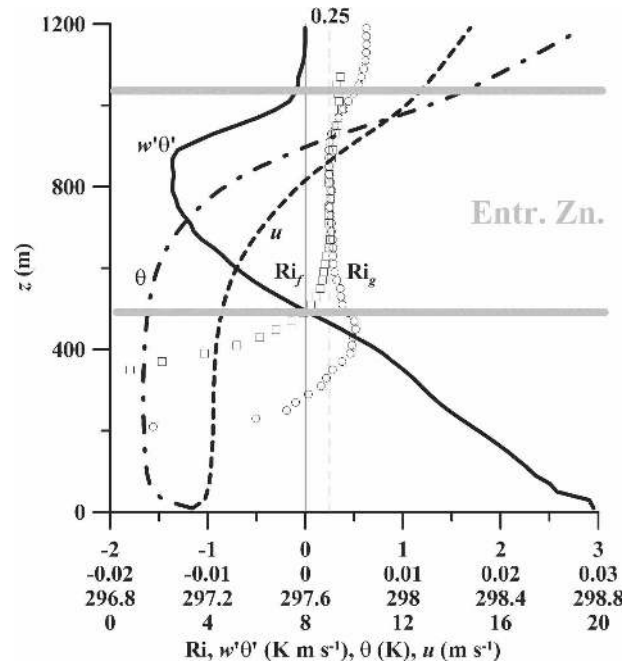FIG. 13. Profiles of gradient Richardson number Ri_g (open circles), flux Richardson number Ri_f (open squares), heat flux (solid black line), potential temperature (dot–dashed line), and the x component of momentum (dashed line) at $t = 15\,000$ s in the GS simulation with $\partial\theta/\partial z = 0.003$ K m^{-1} and $Q_s = 0.03$ K m s^{-1}.

enable identification of the entrainment zone boundaries.

The most striking features in these plots are the layers of nearly constant Ri_g and Ri_f over much of the entrainment zone [see also Ri_g profiles in Kim et al. (2003)]. In the GS case (Fig. 13), $Ri_f \approx Ri_g \approx 0.25$ over a layer approximately 300 m deep, so this layer is reasonably well resolved on the LES grid. The GC simulation also features a layer of constant Ri inside the entrainment zone, with $Ri_f \approx Ri_g \approx 0.25$ (see Fig. 12). In both layers, Ri_g stays nearly constant with height, while the velocity and potential temperature profiles are rather curved. Thus, Ri_g remains constant in the face of changing shear and temperature stratification.

Not all simulated CBLs contain the layer of constant Ri_g in the entrainment zone. In many instances, the horizontal extent of $Ri_g < 0.25$ at the CBL top may not be large enough for a $Ri_g \approx 0.25$ layer to appear in the mean profiles. In other cases, the CBL growth is too fast to allow much accumulation of shear in the entrainment zone. Perhaps some more consistent behavior of Ri_g could be demonstrated if a Lilly (2002a,b) type coordinate system were used for averaging, but our efforts to make the required coordinate transformation with the LES data were not fruitful.

If Ri_f is used in place of Ri_g, many of the cases come closer together, as demonstrated in Fig. 14 for the GC cases. This suggests a balance between the shear production and buoyancy destruction in the entrainment zone (Mahrt and Lenschow 1976) that may be better described by Ri_f than by Ri_g. In the cases where $Ri_g > 0.25$ but $Ri_f \approx 0.25$, the entrainment zone turbulence may not be driven by KH instabilities as much as by the buoyancy flux from below, but the buoyancy-produced turbulence may still be driving the momentum flux (because of the strong entrainment) to an extent that the shear production of turbulence remains relatively important. For example, in the case with $Q_s = 0.3$ K m s^{-1} and $\partial\theta/\partial z = 0.010$ K m^{-1}, $Ri_g \approx 0.8$, which is barely in a turbulence-supporting range, while $Ri_f \approx 0.4$, pointing to the shear production of TKE being relatively important in the entrainment zone. We found that, overall, for the cases in which shear plays a role in speeding the rate of CBL growth, $Ri_f \lesssim 0.4$ at z_i.

Within the set of GS simulations, Ri_f appears slightly dependent on the free atmosphere stratification, as shown in Fig. 15. For the GS cases with moderate background stratification ($\partial\theta/\partial z = 0.003$ K m^{-1}), the Ri_f values approach 0.25 very quickly and then stay at this level. For the strongest stratification, Ri_f starts out large
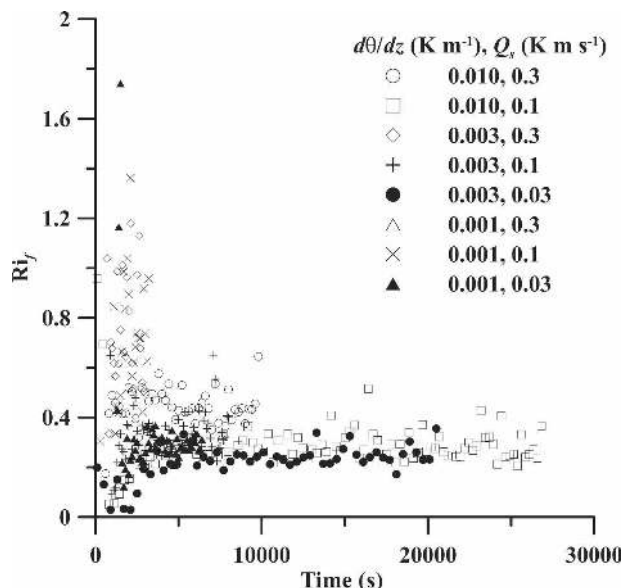
FIG. 14. Flux Richardson number Ri_f at $z = z_i$ as a function of time for all simulated GC cases. The simulations are labeled with the following symbols: $\partial\theta/\partial z = 0.010$ K m^{-1}, $Q_s = 0.30$ K m s^{-1} (open circles); $\partial\theta/\partial z = 0.010$ K m^{-1}, $Q_s = 0.10$ K m s^{-1} (open squares); $\partial\theta/\partial z = 0.003$ K m^{-1}, $Q_s = 0.30$ K m s^{-1} (open diamonds); $\partial\theta/\partial z = 0.003$ K m^{-1}, $Q_s = 0.10$ K m s^{-1} (plusses); $\partial\theta/\partial z = 0.003$ K m^{-1}, $Q_s = 0.03$ K m s^{-1} (solid circles); $\partial\theta/\partial z = 0.001$ K m^{-1}, $Q_s = 0.30$ K m s^{-1} (open triangles); $\partial\theta/\partial z = 0.001$ K m^{-1}, $Q_s = 0.10$ K m s^{-1} (crosses); $\partial\theta/\partial z = 0.001$ K m^{-1}, $Q_s = 0.03$ K m s^{-1} (solid triangles).

FIG. 15. Flux Richardson number Ri_f at $z = z_i$ as a function of time for all simulated GS cases. For notation, see Fig. 14.

and asymptotically decreases to $Ri_f = 0.25$ over the course of the simulation.

g. Fraction of shear-generated TKE available for entrainment

Finally, following the methodology outlined in section 3c, we quantitatively evaluate the fraction of the shear-produced TKE spent on the negative buoyancy flux of entrainment C_P. In a way, this fraction has an analogous meaning for shear-generated TKE that the ratio C_1 has for buoyancy-generated TKE in shear-free CBLs.

Owing to the strong finescale variability of the profiles of the TKE shear and buoyancy production, each data point in the time series was averaged with the surrounding ten data points (five on each side) before plotting. In most sheared CBL cases (Figs. 16 and 17), the average fraction appears to fall between 0.3 and 0.5, occasionally dropping down to 0.2. This is much less than the 0.7 value that Price et al. (1978) suggested and Tennekes and Driedonks (1981), Driedonks (1982), and Pino et al. (2003) used in their analyses of entrainment. Atmospheric data in Fig. 9 of Brost et al. (1982b)
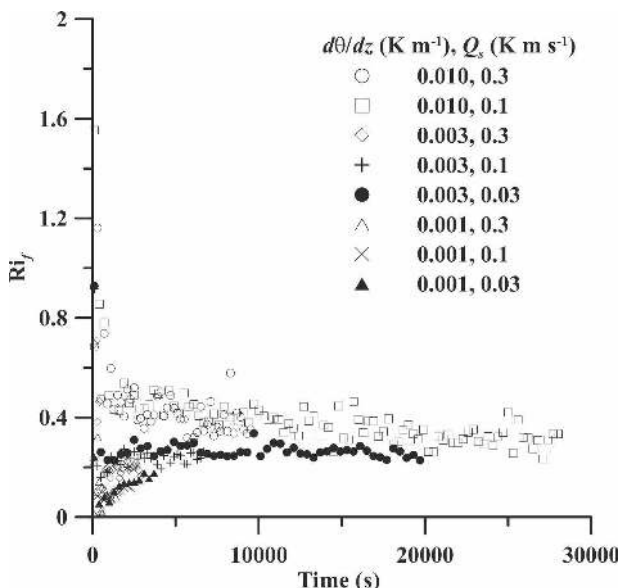
show that the fraction may fall somewhere between 0.7 and 0.2. It is certainly evident, looking at both the LES and atmospheric data, that many data points are required to make a reasonable estimate of this fraction. Also, the GC cases appear to have an overall lower shear-utilization efficiency (smaller fraction of shear-generated TKE available for entrainment, see Fig. 16) than the GS cases (Fig. 17), which suggests that the analysis technique for integral shear production does not fully exclude the effects of surface shear in the GC cases. At the same time, this provides further evidence that surface layer shear does not directly impact entrainment.

5. Conclusions

In the reported study, LES was used as a tool to investigate the dynamics of sheared CBL entrainment in a wide variety of atmospheric conditions. The main conclusions reached in the study are the following.

First, the surface layer shear seems to play little, if any, direct role in the enhancement of entrainment in sheared CBLs. This conclusion supports findings from previous studies (Lenschow 1970, 1974; Deardorff and Willis 1982; Moeng and Sullivan 1994), which have suggested that most of the surface shear-generated TKE dissipates locally. On the other hand, the surface shear has an indirect effect on entrainment by slowing the flow in the CBL interior and causing development of shear at the top of the CBL, and it is this entrainment
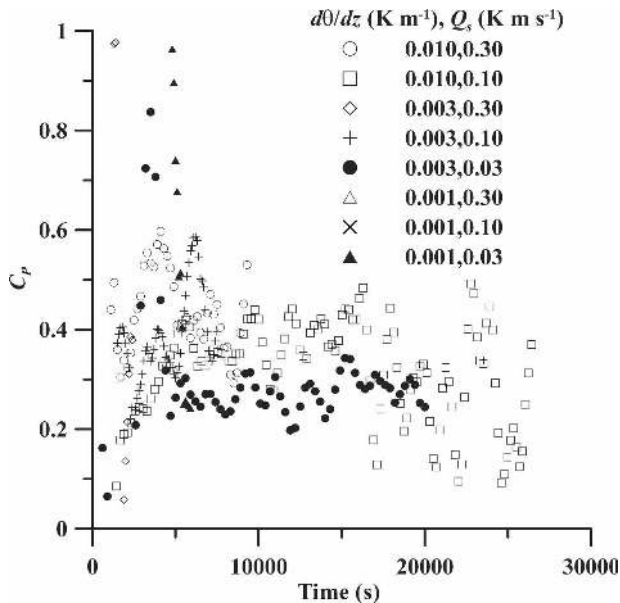
FIG. 16. The fraction of entrainment zone sheared-produced TKE used for entrainment in the GC case CBLs. The fraction was calculated by performing the integration illustrated in Fig. 5, which compared the integral change in the buoyancy flux profile expected from the NS case with the integral shear production in the entrainment zone and upper portion of the mixed layer. The output at all data points was averaged using the data point and five adjacent data points each on either side. For notation, see Fig. 14.

FIG. 17. The fraction of entrainment zone sheared-produced TKE used for entrainment for the GS case CBLs. For notation, see Figs. 14 and 16.

zone shear that enhances the entrainment. In some of the GC cases, which were designed to evaluate the effects of surface shear on entrainment, the enhancement of entrainment equaled or exceeded that of the GS cases, which had geostrophic shear. This only happened when the shear production of TKE in the entrainment zone of the GC case CBLs was as strong as or stronger than it was in the GS case CBLs.

Second, many of the simulated sheared CBLs were found to exhibit a layer of nearly constant gradient Richardson number Ri_g in the entrainment zone. The value of $Ri_g \approx 0.25$ was approached when the shear production of TKE in the entrainment zone was significant compared to the buoyancy production of turbulence. If the flux Richardson number Ri_f was used as a benchmark, its value was consistently within the range $0.2 \leq Ri_f \leq 0.4$ whenever shear enhancement of CBL growth was observed. The local constancy of Ri_f within the entrainment zone appears to manifest a balance between the mechanism of turbulence generation by shear and the turbulence destruction mechanism associated with negative buoyancy flux, dissipation, or energy drain out of the entrainment zone.

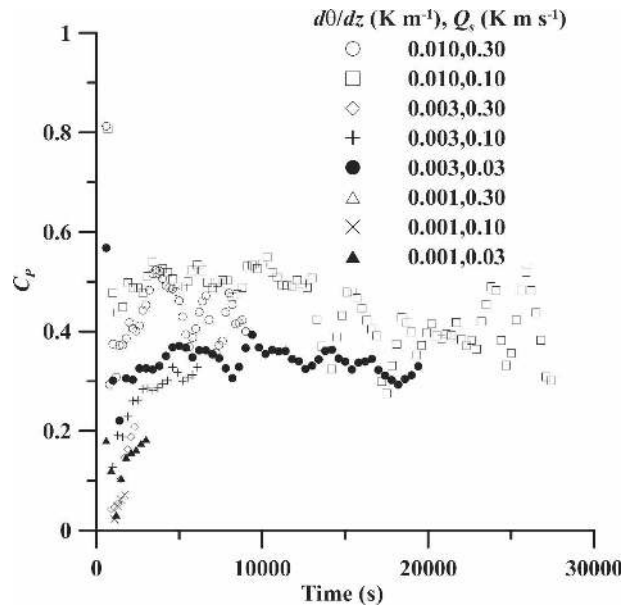If enough shear accumulates in the entrainment zone to disrupt the balance ($Ri_f < 0.25$), the shear-generated

TKE will tend to increase the depth of the layer to the point where the integral negative buoyancy flux (entrainment) and dissipation increase to restore the balance. If the layer deepens to the point that $Ri_f > 0.25$, or the shear decreases, the turbulence intensity fades, and the layer collapses so that the balance is restored. Our LES results indicate that this balance exists locally, but it appears to occur over a sufficiently large depth that it could be considered an integral balance over the whole layer. The numerical results also show that Ri_f at z_i tends to approach 0.25 in all the simulated sheared CBL cases.

Third, the fraction of the shear-produced TKE used for entrainment was found to be no higher than 0.5 in the simulations, once the entrainment reaches a relatively steady state. This suggests that fractions of 0.7 or higher, used in Price et al. (1978), Tennekes and Driedonks (1981), Driedonks (1982), Boers et al. (1984), and Pino et al. (2003), are probably overestimates. In Part II of this paper (Conzemius and Fedorovich 2006), the bulk-model entrainment equations, which take into account this fraction of shear-generated TKE available for entrainment, will be tested against the LES data.

The derived conclusions above need to be tested more fully against atmospheric data. In particular, the numerical scheme in the LES code used in this study (Asselin 1972; Durran 1999) is rather dissipative at the smallest resolved scales of motion, but analysis of the cospectra of the turbulent vertical potential tempera-

ture flux shows that the largest scales of motion (Schmidt and Schumann 1989; Kaiser and Fedorovich 1998), which are well-resolved on the grid, are responsible for most of the entrainment. Also, a recently organized comparison exercise for a sample of GS and GC case CBLs (Fedorovich et al. 2004c) showed little substantial differences among the entrainment predictions of several different LES codes based on rather different advection–diffusion schemes. Nevertheless, simulating higher-order features of turbulence in the entrainment zone (Otte and Wyngaard 2001) would best be done with higher-order numerics.

The relatively low resolution of routine measurements and the expense of higher-resolution experimental measurements have prevented a large number of atmospheric sheared CBL studies from being conducted to date. Nevertheless, the technology for remote sensing of temperature and wind in the CBL is rapidly advancing. For instance, the existing 915-MHz profiler technology is allowing vertical resolution down to 60 m or less (White and Senff 1999: Cohn and Angevine 2000; Bianco and Wilczak 2002; Lambert et al. 2003), and the recent International H_2O Project (Weckwerth et al. 2004) deployed a substantial array of profilers and radars to study the CBL structure. Future experiments may provide more useful data to test the results of the current study if they are designed specifically to look at entrainment processes at the CBL top.

While the present study focused on the dynamics of sheared CBLs in a statistical sense, one particularly interesting aspect of the simulated CBLs in this study is the difference in turbulence structures among the NS, GS, and GC cases, ranging from quasi-hexagonal cells in the NS case to horizontal convective rolls (Weckwerth et al. 1996, 1997, 1999) in the GC case CBLs. It would be interesting to further examine what role such organized structures play in the momentum and buoyancy transport in the sheared (GC case) CBLs and how they influence the horizontal distribution of shear in the entrainment zone.

REFERENCES

Angevine, W. M., 1999: Entrainment results including advection and case studies from the Flatland boundary layer experiments. *J. Geophys. Res.,* **104,** 30 947–30 963.

——, H. K. Baltink, and F. C. Bosveld, 2001: Observations of the morning transition of the convective boundary layer. *Bound.-Layer Meteor.,* **101,** 209–227.

Arya, S. P. S., and J. C. Wyngaard, 1975: Effect of baroclinicity on wind profiles and the geostrophic drag law for the convective planetary boundary layer. *J. Atmos. Sci.,* **32,** 767–778.

Asselin, R., 1972: Frequency filter for time integrations. *Mon. Wea. Rev.,* **100,** 487–490.

Ayotte, K. W., and Coauthors, 1996: An evaluation of neutral and convective planetary boundary-layer parameterizations relative to large eddy simulations. *Bound.-Layer Meteor.,* **79,** 131–175.

Ball, F. K., 1960: Control of inversion height by surface heating. *Quart. J. Roy. Meteor. Soc.,* **86,** 483–494.

Barr, A. G., and G. S. Strong, 1996: Estimating regional surface heat and moisture fluxes above prairie cropland from surface and upper-air measurements. *J. Appl. Meteor.,* **35,** 1716–1735.

Batchvarova, E., and S.-E. Gryning, 1991: Applied model for the growth of the daytime mixed layer. *Bound.-Layer Meteor.,* **56,** 261–274.

——, and ——, 1994: An applied model for the height of the daytime mixed layer and the entrainment zone. *Bound.-Layer Meteor.,* **71,** 311–323.

Betts, A. K., 1973: Non-precipitating cumulus convection and its parameterization. *Quart. J. Roy. Meteor. Soc.,* **99,** 178–196.

——, 1974: Reply to comment on the paper "Non-precipitating Cumulus Convection and its Parameterization." *Quart. J. Roy. Meteor. Soc.,* **100,** 469–471.

——, and J. H. Ball, 1994: Budget analysis of FIFE 1987 sonde data. *J. Geophys. Res.,* **99,** 3655–3666.

——, and A. G. Barr, 1996: First International Satellite Land Surface Climatology Field Experiment 1987 sonde budget revisited. *J. Geophys. Res.,* **101,** 23 285–23 288.

——, R. L. Desjardins, and J. I. MacPherson, 1992: Budget analysis of the boundary layer grid flights during FIFE 1987. *J. Geophys. Res.,* **97,** 18 533–18 546.

Bianco, L., and J. M. Wilczak, 2002: Convective boundary layer depth: Improved measurement by Doppler radar wind profiler using fuzzy logic methods. *J. Atmos. Oceanic Technol.,* **19,** 1745–1758.

Boers, R., E. W. Eloranta, and R. L. Coulter, 1984: Lidar observations of mixed layer dynamics: Tests of parameterized entrainment models of mixed layer growth rate. *J. Climate Appl. Meteor.,* **23,** 247–266.

Brost, R. A., D. H. Lenschow, and J. C. Wyngaard, 1982a: Marine stratocumulus layers. Part I: Mean conditions. *J. Atmos. Sci.,* **39,** 800–817.

——, ——, and ——, 1982b: Marine stratocumulus layers. Part II: Turbulence budgets. *J. Atmos. Sci.,* **39,** 818–836.

Brown, A. R., 1996: Large-eddy simulation and parametrization

of the baroclinic boundary-layer. *Quart. J. Roy. Meteor. Soc.,* **122,** 1779–1798.

Carson, D. J., 1973: The development of dry inversion-capped convectively unstable boundary layer. *Quart. J. Roy. Meteor. Soc.,* **99,** 450–467.

Caughey, S. J., and S. G. Palmer, 1979: Some aspects of turbulence structure through the depth of the convective boundary layer. *Quart. J. Roy. Meteor. Soc.,* **105,** 811–827.

Chou, S.-H., D. Atlas, and E.-N. Yeh, 1986: Turbulence in a convective marine atmospheric boundary layer. *J. Atmos. Sci.,* **43,** 547–564.

Cohn, S. A., and W. M. Angevine, 2000: Boundary layer height and entrainment zone thickness measured by lidars and wind-profiling radars. *J. Appl. Meteor.,* **39,** 1233–1247.

Conzemius, R. J., and E. Fedorovich, 2006: Dynamics of sheared convective boundary layer entrainment. Part II: Evaluation of bulk model predictions of entrainment flux. *J. Atmos. Sci.* **63,** 1179–1199.

Davis, K. J., D. H. Lenschow, S. P. Oncley, C. Kiemle, G. Ehret, A. Giez, and J. Mann, 1997: Role of entrainment in surface–atmosphere interactions over the boreal forest. *J. Geophys. Res.,* **102,** 29 219–29 230.

Deardorff, J. W., 1970a: Preliminary results from numerical integration of the unstable boundary layer. *J. Atmos. Sci.,* **27,** 1209–1211.

——, 1970b: Convective velocity and temperature scales for the unstable planetary boundary layer and for Raleigh convection. *J. Atmos. Sci.,* **27,** 1211–1213.

——, 1972: Numerical investigation of neutral and unstable planetary boundary layers. *J. Atmos. Sci.,* **29,** 91–115.

——, 1974: Three dimensional numerical study of turbulence in an entraining mixed layer. *Bound.-Layer Meteor.,* **7,** 199–226.

——, 1979: Prediction of convective mixed-layer entrainment for realistic capping inversion structure. *J. Atmos. Sci.,* **36,** 424–436.

——, 1980: Stratocumulus-capped mixed layers derived from a three-dimensional model. *Bound.-Layer Meteor.,* **18,** 495–527.

——, and G. E. Willis, 1982: Dependence of mixed-layer entrainment on shear stress and velocity jump. *J. Fluid Mech.,* **115,** 123–140.

——, and ——, 1985: Further results from a laboratory model of the convective planetary boundary layer. *Bound.-Layer Meteor.,* **32,** 205–236.

——, ——, and D. K. Lilly, 1969: Laboratory investigation of nonsteady penetrative convection. *J. Fluid Mech.,* **35,** 7–31.

——, ——, and B. H. Stockton, 1980: Laboratory studies of the entrainment zone of a convectively mixed layer. *J. Fluid Mech.,* **100,** 41–64.

Driedonks, A. G. M., 1982: Models and observations of the growth of the atmospheric boundary layer. *Bound.-Layer Meteor.,* **23,** 283–306.

Durran, D. R., 1999: *Numerical Methods for Wave Equations in Geophysical Fluid Dynamics.* Springer-Verlag, 465 pp.

Fedorovich, E., 1995: Modeling the atmospheric convective boundary layer within a zero-order jump approach: An extended theoretical framework. *J. Appl. Meteor.,* **34,** 1916–1928.

——, and D. V. Mironov, 1995: A model for a shear-free convective boundary layer with parameterized capping inversion structure. *J. Atmos. Sci.,* **52,** 83–95.

——, and R. Kaiser, 1998: Wind tunnel model study of turbulence regime in the atmospheric convective boundary layer. *Buoy-*

ant Convection in Geophysical Flows, E. J. Plate et al., Eds., Kluwer, 327–370.

——, and J. Thäter, 2001: Vertical transport of heat and momentum across a sheared density interface at the top of a horizontally evolving convective boundary layer. *J. Turbul.,* **2,** doi:10.1088/1468-5248/2/1/007.

——, R. Kaiser, M. Rau, and E. Plate, 1996: Wind tunnel study of turbulent flow structure in the convective boundary layer capped by a temperature inversion. *J. Atmos. Sci.,* **53,** 1273–1289.

——, F. T. M. Nieuwstadt, and R. Kaiser, 2001a: Numerical and laboratory study of horizontally evolving convective boundary layer. Part I: Transition regimes and development of the mixed layer. *J. Atmos. Sci.,* **58,** 70–86.

——, ——, and ——, 2001b: Numerical and laboratory study of horizontally evolving convective boundary layer. Part II: Effects of elevated wind shear and surface roughness. *J. Atmos. Sci.,* **58,** 546–560.

——, R. Conzemius, and D. Mironov, 2004a: Convective entrainment into a shear-free, linearly stratified atmosphere: Bulk models reevaluated through large eddy simulations. *J. Atmos. Sci.,* **61,** 281–295.

——, ——, and A. Shapiro, 2004b: Nonstationarity of convective boundary layer growth in a heterogeneously stratified, shear-free atmosphere. Preprints, *16th Symp. on Boundary Layers and Turbulence*, Portland, ME, Amer. Meteor. Soc., CD-ROM, P7.9.

——, and Coauthors, 2004c: Entrainment into sheared convective boundary layers as predicted by different large eddy simulation codes. Preprints, *16th Symp. on Boundary Layers and Turbulence*, Portland, ME, Amer. Meteor. Soc., CD-ROM, P4.7.

Flamant, C., J. Pelon, P. H. Flamant, and P. Durand, 1997: Lidar determination of the entrainment zone thickness at the top of the unstable marine atmospheric boundary layer. *Bound.-Layer Meteor.,* **83,** 247–284.

Garratt, J. R., and J. C. Wyngaard, 1982: Winds in the atmospheric convective boundary layer—Prediction and observation. *J. Atmos. Sci.,* **39,** 1307–1316.

Grossman, R. L., 1992: Convective boundary layer budgets of moisture and sensible heat over an unstressed prairie. *J. Geophys. Res.,* **97,** 18 425–18 438.

Holtslag, A. A. M., and P. G. Duynkerke, Eds., 1998: *Clear and Cloudy Boundary Layers.* Royal Netherlands Academy of Arts and Sciences, 372 pp.

Hoxit, L. R., 1974: Planetary boundary layer winds in baroclinic conditions. *J. Atmos. Sci.,* **31,** 1003–1020.

Hunt, J. C. R., and P. A. Durbin, 1999: Perturbed vortical layers and shear sheltering. *Fluid Dyn. Res.,* **24,** 375–404.

Kaimal, J. C., J. C. Wyngaard, D. A. Haugen, O. R. Coté, Y. Izumi, S. J. Caughey, and C. J. Readings, 1976: Turbulence structure in a convective boundary layer. *J. Atmos. Sci.,* **33,** 2152–2169.

Kaiser, R., and E. Fedorovich, 1998: Turbulence spectra and dissipation rates in a wind tunnel model of the atmospheric convective boundary layer. *J. Atmos. Sci.,* **55,** 580–594.

Kato, H., and O. M. Phillips, 1969: On the penetration of a turbulent layer into stratified fluid. *J. Fluid Mech.,* **37,** 643–655.

Khanna, S., and J. G. Brasseur, 1998: Three-dimensional buoyancy and shear-induced local structure of the atmospheric boundary layer. *J. Atmos. Sci.,* **55,** 710–743.

Kiemle, C., M. Kaestner, and G. Ehret, 1995: The convective boundary layer structure from lidar and radiosonde measure-

ments during the EFEDA '91 campaign. *J. Atmos. Oceanic Technol., 12,* 771–782.

Kim, S.-W., and S.-U. Park, 2003: Coherent structures near the surface in a strongly sheared convective boundary layer generalized by large-eddy simulation. *Bound.-Layer Meteor., 106,* 35–60.

——, ——, and C.-H. Moeng, 2003: Entrainment processes in the convective boundary layer with varying wind shear. *Bound.-Layer Meteor., 108,* 221–245.

Kundu, P. K., 1990: *Fluid Mechanics.* Academic Press, 638 pp.

Lambert, W. C., F. J. Merceret, G. E. Taylor, and J. G. Ward, 2003: Performance of five 915-MHz wind profilers and an associated automated quality control algorithm in an operational environment. *J. Atmos. Oceanic Technol., 20,* 1488–1495.

LeMone, M. A., 1973: The structure and dynamics of horizontal roll vortices in the planetary boundary layer. *J. Atmos. Sci., 30,* 1077–1091.

——, M. Zhou, C.-H. Moeng, D. H. Lenschow, L. J. Miller, and R. L. Grossman, 1999: An observational study of wind profiles in the baroclinic convective mixed layer. *Bound.-Layer Meteor., 90,* 47–82.

Lenschow, D. H., 1970: Airplane measurements of planetary boundary layer structure. *J. Appl. Meteor., 9,* 874–884.

——, 1974: Model of the height variation of the turbulence kinetic energy budget in the unstable planetary boundary layer. *J. Atmos. Sci., 31,* 465–474.

——, J. C. Wyngaard, and W. T. Pennell, 1980: Mean-field and second-moment budgets in a baroclinic, convective boundary layer. *J. Atmos. Sci., 37,* 1313–1326.

Lewellen, D. C., and W. S. Lewellen, 1998: Large-eddy boundary layer entrainment. *J. Atmos. Sci., 55,* 2645–2665.

Lilly, D. K., 1968: Models of cloud-topped mixed layers under a strong inversion. *Quart. J. Roy. Meteor. Soc., 94,* 292–309.

——, 2002a: Entrainment into mixed layers. Part I: Sharp-edged and smooth-edged tops. *J. Atmos. Sci., 59,* 3340–3352.

——, 2002b: Entrainment into mixed layers. Part II: A new closure. *J. Atmos. Sci., 59,* 3353–3361.

Long, R. R., 1975: The influence of shear on mixing across density interfaces. *J. Fluid Mech., 70,* 305–320.

Lyons, T., and B. Scott, 1990: *Air Pollution Meteorology.* CRC Press, 224 pp.

Mahrt, L., and D. H. Lenschow, 1976: Growth dynamics of the convectively mixed layer. *J. Atmos. Sci., 33,* 41–51.

Manins, P. C., and J. S. Turner, 1978: The relation between flux ratio and energy ratio in convectively mixed layers. *Quart. J. Roy. Meteor. Soc., 104,* 39–44.

Margulis, S. A., and D. Entekhabi, 2004: Boundary-layer entrainment estimation through assimilation of radiosonde and micrometeorological data into a mixed layer model. *Bound.-Layer Meteor., 110,* 405–433.

Mason, P. J., 1989: Large-eddy simulation of the convective atmospheric boundary layer. *J. Atmos. Sci., 46,* 1492–1516.

Moeng, C.-H., and J. C. Wyngaard, 1984: Statistics of conservative scalars in the convective boundary layer. *J. Atmos. Sci., 41,* 3161–3169.

——, and ——, 1989: Evaluation of turbulent transport and dissipation closures in second-order modeling. *J. Atmos. Sci., 46,* 2311–2330.

——, and P. P. Sullivan, 1994: A comparison of shear- and buoyancy-driven planetary boundary layer flows. *J. Atmos. Sci., 51,* 999–1022.

Otte, M. J., and J. C. Wyngaard, 2001: Stably stratified interfacial-

layer turbulence from large eddy simulation. *J. Atmos. Sci., 58,* 3424–3442.

Pennel, W. T., and M. A. LeMone, 1974: An experimental study of turbulence in the fair-weather trade wind boundary layer. *J. Atmos. Sci., 31,* 1308–1323.

Pino, D., J. V.-G. de Arellano, and P. J. Duynkerke, 2003: The contribution of shear to the evolution of a convective boundary layer. *J. Atmos. Sci., 60,* 1913–1926.

Pope, S. B., 2000: *Turbulent Flows.* Cambridge University Press, 771 pp.

Price, J. F., C. N. K. Mooers, and J. C. van Leer, 1978: Observation and simulation of storm-induced mixed layer deepening. *J. Phys. Oceanogr., 8,* 582–599.

Randall, D. A., and W. H. Schubert, 2004: Dreams of a stratocumulus sleeper. *Turbulence and Mesoscale Meteorology*, Cambridge University Press, 71–94.

Schmidt, H., and U. Schumann, 1989: Coherent structure of the convective boundary layer derived from large eddy simulations. *J. Fluid Mech., 200,* 511–562.

Schneider, J. M., and D. K. Lilly, 1999: An observational and numerical study of a sheared, convective boundary layer. Part I: Phoenix II observations, statistical description, and visualization. *J. Atmos. Sci., 56,* 3059–3078.

Sorbjan, Z., 1996a: Numerical study of penetrative and "solid lid" nonpenetrative convective boundary layers. *J. Atmos. Sci., 53,* 101–112.

——, 1996b: Effects cause by varying the strength of the capping inversion based on a large eddy simulation model of the shear-free convective boundary layer. *J. Atmos. Sci., 53,* 2015–2024.

——, 2004: Large-eddy simulation of the baroclinic mixed layer. *Bound.-Layer Meteor., 112,* 57–80.

Stage, S. A., and J. A. Businger, 1981: A model for entrainment into a cloud-topped marine boundary layer. Part I: Model description and application to a cold-air outbreak episode. *J. Atmos. Sci., 38,* 2213–2229.

Stull, R. B., 1973: Inversion rise model based on penetrative convection. *J. Atmos. Sci., 30,* 1092–1099.

——, 1976a: The energetics of entrainment across a density interface. *J. Atmos. Sci., 33,* 1260–1267.

——, 1976b: Internal gravity waves generated by penetrative convection. *J. Atmos. Sci., 33,* 1279–1286.

——, 1976c: Mixed-layer depth model based on turbulent energetics. *J. Atmos. Sci., 33,* 1268–1278.

——, 1988: *An Introduction to Boundary Layer Meteorology.* Kluwer, 670 pp.

Sullivan, P., C.-H. Moeng, B. Stevens, D. H. Lenschow, and S. D. Mayor, 1998: Structure of the entrainment zone capping the convective atmospheric boundary layer. *J. Atmos. Sci., 55,* 3042–3064.

Sykes, R. I., and D. S. Henn, 1989: Large-eddy simulation of turbulent sheared convection. *J. Atmos. Sci., 46,* 1106–1118.

Tennekes, H., 1973: A model for the dynamics of the inversion above a convective boundary layer. *J. Atmos. Sci., 30,* 558–567.

——, and A. G. M. Driedonks, 1981: Basic entrainment equations for the atmospheric boundary layer. *Bound.-Layer Meteor., 20,* 515–531.

Turner, J. S., 1965: The coupled turbulent transports of salt and heat across a sharp density interface. *Int. J. Heat Mass Transfer, 8,* 759–767.

——, 1968: The influence of molecular diffusivity on turbulent

entrainment across a density interface. *J. Fluid Mech.,* **33,** 639–656.

vanZanten, M. C., P. G. Duynkerke, and J. W. M. Cuijpers, 1999: Entrainment parameterization in convective boundary layers. *J. Atmos. Sci.,* **56,** 813–828.

Wallace, J. M., and P. V. Hobbs, 1977: *Atmospheric Science: An Introductory Survey.* Academic Press, 467 pp.

Weckwerth, T. M., J. W. Wilson, and R. M. Wakimoto, 1996: Thermodynamic variability within the convective boundary layer due to horizontal convective rolls. *Mon. Wea. Rev.,* **124,** 769–784.

——, ——, ——, and N. A. Crook, 1997: Horizontal convective rolls: Determining the environmental conditions supporting their existence and characteristics. *Mon. Wea. Rev.,* **125,** 505–526.

——, T. W. Horst, and J. W. Wilson, 1999: An observational study of the evolution of horizontal convective rolls. *Mon. Wea. Rev.,* **127,** 2160–2179.

——, and Coauthors, 2004: An overview of the International H$_2$O Project (IHOP_2002) and some preliminary highlights. *Bull. Amer. Meteor. Soc.,* **85,** 253–277.

White, A. B., and C. J. Senff, 1999: A comparison of mixing depths observed by ground-based wind profilers and an airborne lidar. *J. Atmos. Oceanic Technol.,* **16,** 584–590.

Willis, G. E., and J. W. Deardorff, 1974: A laboratory model of the unstable planetary boundary layer. *J. Atmos. Sci.,* **31,** 1297–1307.

Wu, J., 1973: Wind-induced turbulent entrainment across a stable density interface. *J. Fluid Mech.,* **61,** 275–287.

Wyngaard, J. C., 1998: Experiment, numerical modeling, numerical simulation, and their roles in the study of convection. *Buoyant Convection in Geophysical Flows,* Kluwer, 239–251.

——, and R. A. Brost, 1984: Top-down and bottom-up diffusion of a scalar in the convective boundary layer. *J. Atmos. Sci.,* **41,** 102–112.

Zeman, O., and H. Tennekes, 1977: Parameterization of the turbulent energy budget at the top of the daytime atmospheric boundary layer. *J. Atmos. Sci.,* **34,** 111–123.

Zilitinkevich, S. S., 1991: *Turbulent Penetrative Convection.* Avebury Technical, 179 pp.